PHYSICAL REVIEW E **107**, 024703 (2023)

Editors' Suggestion

Chemical Leslie effect in a chiral smectic-$C^{\star}$ film: Nonsingular target patterns

Félix Bunel[*] and Patrick Oswald[†]
Ens de Lyon, CNRS, Laboratoire de physique, F-69342 Lyon, France

(Received 2 September 2022; accepted 30 November 2022; published 22 February 2023)

We analyze experimentally and theoretically the winding and unwinding of the $\vec{c}$ director in a chiral smectic-$C^{\star}$ film crossed by an ethanol flow. This leads to a target pattern under crossed polarizers when the +1 defect imposed by the boundary conditions is pinned on the edge of the film. We show that the target is deformed at the center of the film when it is subjected to a flow of ethanol because of the presence of two recirculation vortices of chemohydrodynamical origin. This deformation and the two vortices disappear during the unwinding of the target when the ethanol flow is stopped. This unambiguously shows that the target deformation is due to the vortices and not to the elastic anisotropy. These two points are confirmed theoretically. An estimate of the two so-called chemomechanical and chemohydrodynamical Leslie coefficients is also derived from this study.

DOI: 10.1103/PhysRevE.107.024703

I. INTRODUCTION

The introduction of chiral molecules into a liquid crystalline phase can give it new properties since certain symmetries, including the mirror symmetries and the center of inversion, are broken. This is the case in the cholesteric phase which is a chiral nematic phase with a spontaneous twist of its director field but also in the smectic-$C^{\star}$ phase studied here, which is the chiral—and so twisted—version of the smectic-*C* phase. The first experimental observation of this symmetry breaking dates back to the pioneering experiments of Lehmann in 1900, who observed the rotation of the internal texture of cholesteric drops when subjected to a temperature gradient [1]. Lehmann also noticed that by changing the chiral impurity, it was possible to change both the sign of the spontaneous twist and the sense of rotation of the drops [2].

If Lehmann understood the role of chirality in the rotation of the drops, he was however unable to explain this effect which bears his name today. It was only much later, in 1968, that Leslie proposed the first theoretical explanation for the Lehmann effect. Based on the symmetries of the cholesteric phase, Leslie demonstrated the existence of a torque proportional to the local temperature gradient acting on the molecules of the liquid crystal (LC) [3]. According to Leslie, this torque makes the molecules rotate, which causes the internal texture of the cholesteric drops observed by Lehmann to also rotate. This explanation was at the time—and until very recently—unanimously accepted by the scientific community and became a veritable paradigm.

It was not less than 40 years after Leslie's discovery that new experiments on the Lehmann effect were performed, first by one of us (P.O.) and Dequidt [4,5], and then a few years later by the groups of Tabe and Sano [6,7]. These authors reproduced Lehmann's original experiment, which they first interpreted within the framework of Leslie's theory [4,5]. After further quantitative studies, it was nevertheless shown that the rotation velocity of the drops could not be explained by Leslie's theory. It was shown, in particular, that the velocities predicted by this theory were much too small [8,9], and sometimes even of the wrong sign in certain cholesteric mixtures [10]. But the final blow to Leslie's theory was given by Ignés-Mullol *et al.* [11] when they discovered that it was also possible to induce rotation in drops of the nematic—and so achiral—phase of a chromonic lyotropic liquid crystal (provided that the director field inside the drops is twisted, as required by symmetries). We mention that the same phenomenon was also observed recently in the nematic phase of a thermotropic LC made of bent-shaped molecules [12,13].

If it is now proven that the Leslie torque cannot explain quantitatively the rotation of the internal texture of the Lehmann drops, it is nevertheless certain that this torque exists. This was shown by one of us (P.O.) and Dequidt by performing a sliding planar sample experiment [4], as originally proposed by Leslie [3]. In this dynamic experiment, the cholesteric was confined between two plates treated for planar sliding anchoring. The experiment showed that in the presence of a thermal gradient perpendicular to the plates, the cholesteric helix was rotating at constant speed, as predicted by Leslie [3]. In this experiment, the Leslie thermomechanical coefficient was directly deduced from the measurement of the rotation velocity of the helix, knowing the rotational viscosity of the LC. The Leslie torque was also measured indirectly in a static experiment first performed by Eber and Janossy in 1982 with a compensated cholesteric phase [14–16] and reproduced later by Dequidt and one of us (P.O.) [17,18]. In this experiment, the director field does not rotate continuously, but is simply distorted by the Leslie torque. The problem here is that another torque, coming from the variation with temperature of both the elastic constants and the spontaneous twist of the cholesteric phase, is added to the thermomechanical torque, which made interpretations delicate and subject to controversy.

Let us conclude this revision on cholesterics by recalling that Leslie's theory also predicts the existence of a

---

[*] Present address: Centre d'études du Ripault 37260 Monts; felix.bunel@CEA.com
[†] patrick.oswald@ens-lyon.fr

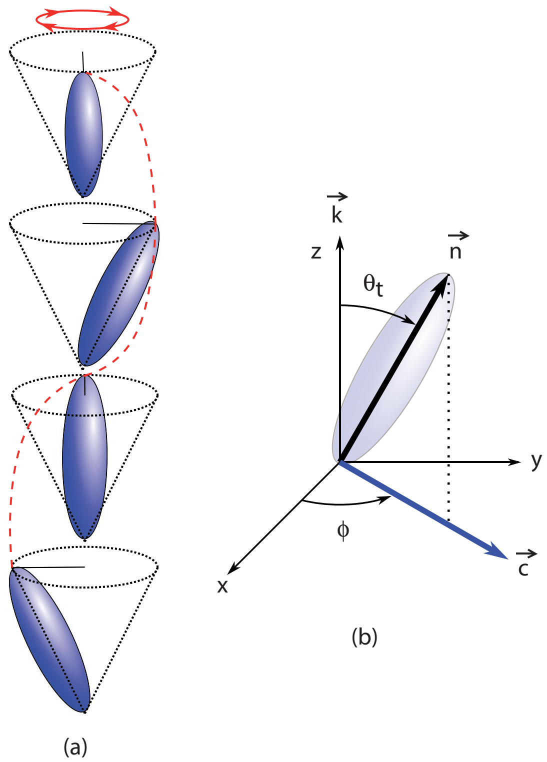

FIG. 1. Structure of the Smectic C⋆ phase (a) and definition of the $\vec{n}$ and $\vec{c}$ directors (b).

thermohydrodynamic effect. To this second effect is associated a stress proportional to the temperature gradient that should cause flows in the samples. To the best of our knowledge, this effect has not yet been observed. We refer the reader to the review article [19] for the description of possible experiments that could be carried out to observe this effect in cholesterics.

We now recall, as noted by de Gennes, that similar effects could be observed in cholesterics when the flow of heat is replaced by a flow of particles or an electric current [20]. In this context, only one experiment was attempted in 1993 by Padmini and Madhusudana [21] to detect the Leslie electromechanical effect. It was nevertheless shown later by Dequidt and one of us (P.O.) that the texture rotation observed by these authors under electric field was not due to a Leslie electromechanical effect, but to the more classical flexoelectric effect [22].

In practice, similar effects should also exist in the smectic-$C^\star$ phase since the director field $\vec{n}$ inside is also twisted as shown in Fig. 1(a). In this figure, $\vec{n}$ gives the average orientation of the LC molecules, $\vec{k}$ is the unit vector normal to the layers, and $\vec{c}$ is the unit vector that gives the orientation of the molecules in the plane of the layers. With these definitions one has

$$\vec{n} = \sin\theta_t \vec{c} + \cos\theta_t \vec{k}, \tag{1}$$

where θ_t is the tilt angle of the molecules with respect to the normal to the layers. Importantly, in a smectic-$C^\star$, $\vec{n}$ and $-\vec{n}$ are equivalent. As a result, all the equations must be invariant under the transformation $(\vec{k}, \vec{c}) \rightarrow (-\vec{k}, -\vec{c})$. To the best of our knowledge, no thermomechanical effects have been reported in the literature so far in this phase. In contrast, there are several experimental evidences for a chemomechanical effect—and to some extent for a chemohydrodynamical effect—in this phase. These effects have been observed in two distinct systems: in chiral Langmuir monolayers when the LC is deposited at the surface of an isotropic liquid (water in general) and in free-standing films of the smectic-$C^\star$ phase. In the two cases, the Leslie effects are due to the presence of a flow of particules accros the films and are thus of chemical nature.

Historically, the chemical Leslie effect was studied experimentally for the first time by Tabe and Yokoyama in 2003 in Langmuir monolayers [23]. It should however be emphasized that the first observation of the rotation of the molecules in such a monolayer is due to Adams *et al.* in 1993 [24]. However, these authors failed to identify the cause of this rotation. In their experiments, Tabe and Yokoyama deposited a chiral LC on the surface of a water-glycerol bath. The molecules, by covering the surface, formed a monolayer with long-range orientational order as in a layer of a smectic-$C^\star$ phase. Observation with a polarized Brewster angle microscope then revealed the formation of concentric rings with the reflected intensity oscillating in the middle of the pattern. These phenomena are due to the rotation of the molecules in large areas of the monolayer when it is subjected to the evaporation flow of the water contained in the subphase. These targetlike patterns were explained as due to the Leslie chemomechanical torque, which is formally equivalent to the thermomechanical torque. In addition, Tabe and Yokoyama showed that the rotation velocity of the molecules in the center of a target was proportional to the water evaporation flow rate and changed sign when the water flow direction was reversed.

The work of Tabe and Yokoyama prompted several researchers to work on the chemical Leslie effect. Starting with Tabe's group that carried out molecular dynamics simulations emulating Langmuir monolayers with different chiral compounds [25,26]. Tsori and de Gennes also published an article on the motion of defects in the targetlike patterns [27] and Svenšek *et al.* performed numerical simulations to show the influence of thermal fluctuations on the observed patterns [28]. In addition, they predicted that spirals should form when the rotation begins with a +1 defect in the center of the zone where the molecules can freely rotate. This prediction was later confirmed experimentally by Gupta *et al.* [29]. Hołyst *et al.* also reproduced Tabe's experiment with new chiral compounds and found that the rotation was not systematic for all of them, contradicting Tabe's initial statement that any chiral liquid crystal [30,31] should feature the Leslie rotation. Finally, we reproduced ourselves these experiments [32] and proposed a complete characterization of the chemomechanical effect in these monolayers by using the Leslie theory.

It must be emphasized that in the Langmuir monolayers, no flow is observed. This is mainly due to the large viscosity of the subphase with respect to the viscosity of the monolayer itself. For this reason, this system is not suitable for studying the chemohydrodynamical effect, i.e., the flows induced by a flux of particles crossing the LC. The situation is different in the free-standing films of smectic-$C^\star$ in which the LC can easily flow. This was demonstrated by Seki and

Tabe in 2011 [33,34]. By subjecting a film to a flow of vapor of alcohol, they observed that the rotation of the molecules was accompanied by flows. They also observed the advection of tracers (small solid particles) deposited on the film and measured the force acting on them using optical tweezers. This method allowed them to estimate the efficiency of the chemohydrodynamical coupling. Unfortunately, their results were not interpreted within the framework of Leslie's theory and the lack of explanations and experimental details on their measurements did not allow such an analysis to be done *a posteriori*.

For this reason, we redid experiments on the freestanding films of smectic-$C^\star$, while seeking to quantify the experimental results as best as possible. We then applied the Leslie theory to explain our results. In practice, we observed two types of patterns. The targetlike pattern already widely mentioned, and another one consisting of spiraling targets partially wound with a $+1$ defect in their center. In this paper, we focus on the nonsingular targetlike pattern, and we refer the reader to a forthcoming paper [35] for the description of the singular spiraling-target-like patterns with a $+1$ defect in the center of the film. We mention here that similar patterns were already observed in nonchiral smectic-C films when the phase winding and the flows are produced by a fiber that pierces the film in its center [36]. To complete our historical survey, we also underline the existence in cholesteric LCs of a diffusomechanical coupling that was interpreted by using the analogy with the Leslie thermo- or chemomechanical coupling [37].

This paper is divided in five sections: A material and methods section (Sec. II), an experimental section (Sec. III), a theoretical section (Sec. IV), a section in which we compare the theoretical and experimental results (Sec. V), and a conclusion (Sec. VI). In Sec. II, we give essential details on the LC chosen and the setup used to stretch, observe and subject the films to a controlled flow of ethanol vapor. In Sec. III, we present the main experimental results concerning the formation of a target pattern when the film is subjected to a flow of ethanol and its disappearance when the flow of ethanol is stopped. Particular attention will be paid to the flows which are present in the film during the phase winding, but also in the stationary regime when the target is formed. In Sec. IV we will recall the equations which govern the dynamics of the film and we will solve them numerically (and analytically when possible) in the framework of a simplified model for the viscosity tensor allowing us to satisfactorily reproduce the experimental results. We will see that, even if the agreement is not perfect, the Leslie theory explains in a convincing way all the experimental results. In Sec. V, a first estimate of the ratio between the chemomechanical and chemohydrodynamical coefficients will be given. Finally, we will summarize our work in the conclusion (Sec. VI) and will present some ways to improve the agreement between theory and experiment.

II. MATERIAL AND METHODS

A. Liquid crystal mixture

All of our measurements were performed with the commercial mixture FELIX M4851-100 (Merck, Germany). This LC has the advantage of being in the Smectic $C^\star$ phase over a wide range of temperature as shown by the phase sequence:

Cr<-20°C–Sm $C^\star$–67°C–Sm A–71°C–Chol–76°C–Iso.

This makes this mixture very easy to use since it is in the Smectic $C^\star$ phase at room temperature. Its main characteristics are given in Ref. [38]. At room temperature (25°C) its pitch is $P \approx 5\ \mu$m, its spontaneous polarization is $P_s \approx 20$ nC/cm^2 and the tilt angle of the molecules in the layers is $\theta_t \approx 28°$.

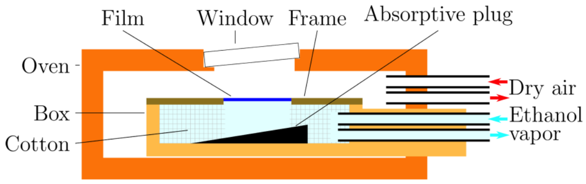

FIG. 2. Oven used in our experiments.

B. Experimental setup

All of our experiments were performed inside a custom-made copper oven (see Fig. 2). Its temperature was fixed at 25 °C and regulated within ±0.1 °C thanks to a RKC CB100 temperature controller (TC Direct, France). The room temperature was kept at a slightly lower temperature, around 21 °C. The film was observed under a reflection microscope (Laborlux 12Pol, Leica) through a glass slide which ensured the thermal insulation of the film. This window was slightly tilted to prevent the light reflected on its surface from entering the microscope objective. A second box with a pinhole fixed on its top was placed inside the oven. The pinhole was purchased from Edmunds Optics (France). Most of our experiments were performed with a pinhole with a diameter of 0.6 mm made in a stainless steel sheet 200 μm thick. As the film attaches to the frame via a meniscus, the result was a film of constant thickness with a slightly smaller diameter, close to 0.5 mm.

To observe the chemical Leslie effects, we chose to subject the film to a flow of ethanol. With this alcohol, these effects are very strong, which made them easy to observe. Moreover, ethanol does not seem to degrade the LC, even over long period of time, which was a valuable asset. Note that we also observed Leslie effects with water, oxygen and nitrogen, but the intensity of the effects observed was much weaker, because these molecules are much less miscible than ethanol in the LC. In contrast, a Leslie effect stronger than with ethanol was observed with acetone, very soluble in the LC, but we did not study it systematically because the films broke very often. In practice, the compositions of the atmospheres inside and outside the box were controlled independently *via* two gas circuits (Fig. 3). More precisely, an air-ethanol mixture was injected inside the box (under the film) and dry air was injected outside (above the film). The air-ethanol mixture was prepared by bubbling dry air (here, synthetic air supplied by a pressurized bottle) in a sealed compartment filled with ethanol. The latter was placed in a Julabo thermostated circulating bath to maintain it at a constant temperature of 18 °C. In this way, we obtained at the outlet air saturated with ethanol vapor at its saturation vapor pressure P_{sat} =5.16 kPa at 18 °C. Note that using a temperature lower than the room temperature (here always close to 21 °C) allowed us to

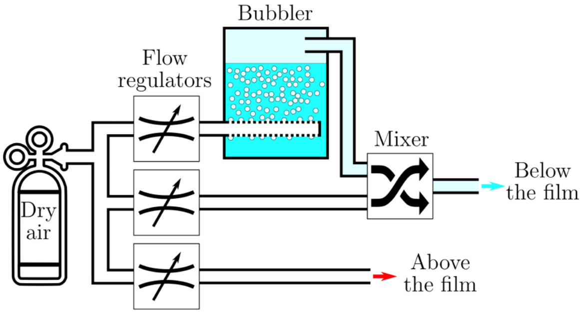

FIG. 3. Scheme of the device used to produce the air-ethanol mixture.

avoid the condensation of ethanol in the rest of the circuit. The ethanol-saturated air was then mixed with dry air in a mixing compartment. Two Bronkhorst EL Select F-201CV mass flow controllers driven by a LabView program made it possible to control the respective flow rates of dry air and air saturated with ethanol at the inlet of the mixer and therefore to precisely set the composition of the mixture. Another Bronkhorst controller made it possible to fix the flow of dry air injected above the film. With this device, it was therefore possible to control both the flow rates above and below the film and the percentage of ethanol vapor in the air injected into the box under the film.

Finally, let us make two remarks on this setup.

First, its proper functioning was checked by replacing ethanol with water and by measuring the humidity at the outlet of the mixer using a precision hygrometer Testoterm 6010. The expected values were in very good agreement with the values given by the hygrometer.

Second and more importantly, we checked that our experimental results were independent of the flow rates of dry air and of ethanol-air mixture injected on either side of the film, at least between 10 and 100 ml/min. To realize the importance of the flow rate, note that the internal volume of the box under the film is of the order of 3 ml. With a flow rate of 50 ml/min, its atmosphere is completely renewed after approximately 4 s. In practice, most of our experiments were performed using a flow rate of 20 ml/min. The box was also filled with cotton to attenuate the air currents inside and therefore limit the parasitic flows in the film as much as possible. With this precaution, no significant flow was observed in the film when dry air was injected on both sides of the film, even at the highest flow rates. These precautions turned out to be fundamental and allow us to affirm that the flows observed in the films are only due to the Leslie forces and/or to the *backflow* effects and are not artifacts due to air currents in the vicinity the film.

Last but not least, we highlight the two reasons why injecting dry air above the film is important. First, because the ethanol vapors that flow through the film must be flushed to maintain the good concentration gradient of ethanol across the film. Second, it was necessary to prevent the water contained in the air of the room from creating an uncontrolled parasitic Leslie effect by diffusing through the film.

In the following, we will use as a control parameter for the chemical Leslie effect the difference in ethanol vapor pressure $\mathcal{P}$ between the two sides of the film. As $\mathcal{P} = 0$ on top of the film, the latter is expressed as

$$\Delta\mathcal{P} = \%\times\mathcal{P}_{\text{sat}}, \tag{2}$$

where % is the percentage of ethanol vapor below the film and $\mathcal{P}_{\text{sat}}$ the saturation vapor pressure of ethanol equal to 5.16 kPa at 18 °C.

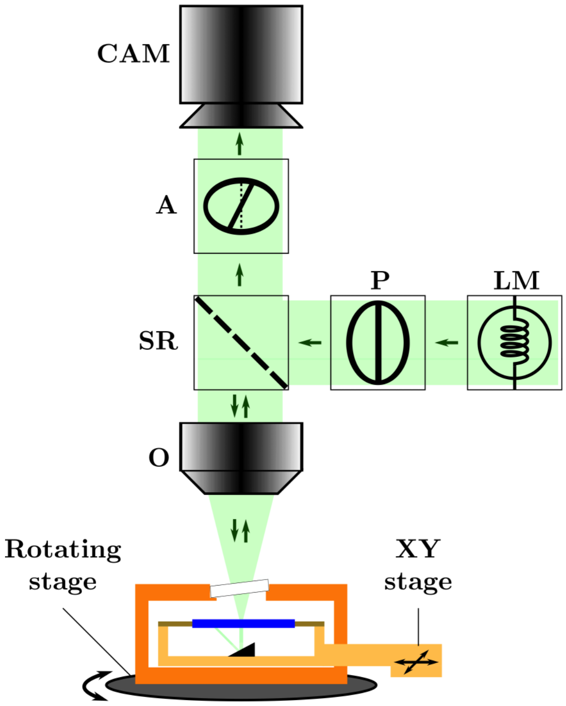

FIG. 4. Diagram of the optical device employed to visualize the film and its texture.

C. Film characterization

To visualize the film and its texture, we used a polarized reflection microscope (see Fig. 4). The film was illuminated with a mercury vapor lamp equipped with a green filter (546 nm) or a blue filter (436 nm). A black absorbent pad, the surface of which is tilted with respect to the horizontal plane, was placed under the film to eliminate all the reflections other than those coming from the film. The position of the film in the oven was adjusted with an XY stage, which made it easy to select the study area. The film could also be rotated at will since the oven was placed on the microscope rotating stage. The images were acquired with an sCMOS camera (Zyla 4.2 MP, Andor) with a resolution of 0.51 µm with a ×10 objective or of 0.25 µm with a ×20 objective. To be sensitive to the orientation of the molecules, the microscope was equipped with a polarizer and an analyzer. We measured the intensity reflected from the film as a function of the orientation of the $\vec{c}$ director. For this purpose, we used a sheet of mylar of thickness 200 µm in which a hole of dimension 4×0.5 mm was drilled. On the sheet, we glued two metal electrodes parallel to the large side of the hole and separated by a distance of 8 mm. Once the film was stretched and equilibrated, the molecules were oriented by applying a DC electric field and the film was then rotated using the microscope rotating stage. As the smectic-$C^{\star}$ phase is ferroelectric with its spontaneous polarization

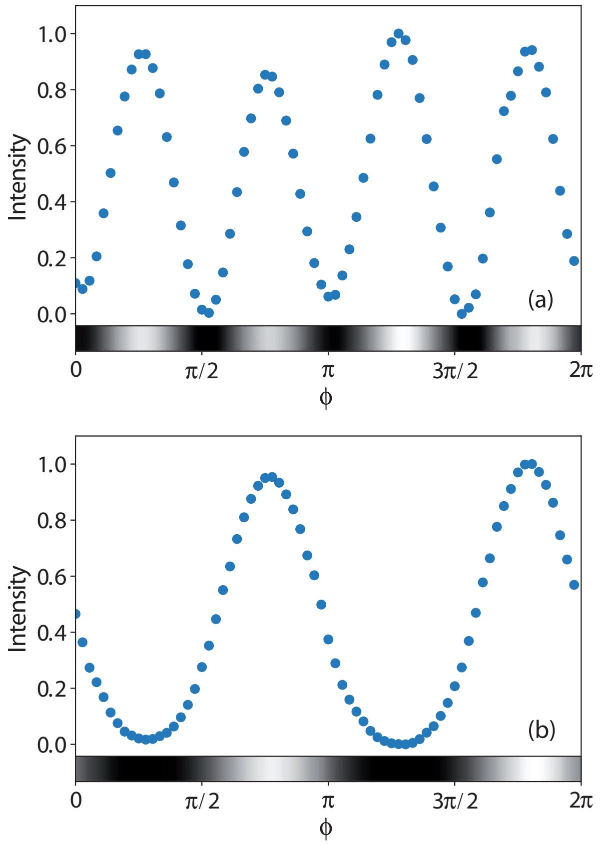

FIG. 5. Reflected intensity as a function of the orientation of the $\vec{c}$ director when the polarizer and the analyzer are crossed (a) and slightly uncrossed by 5 ° (b).

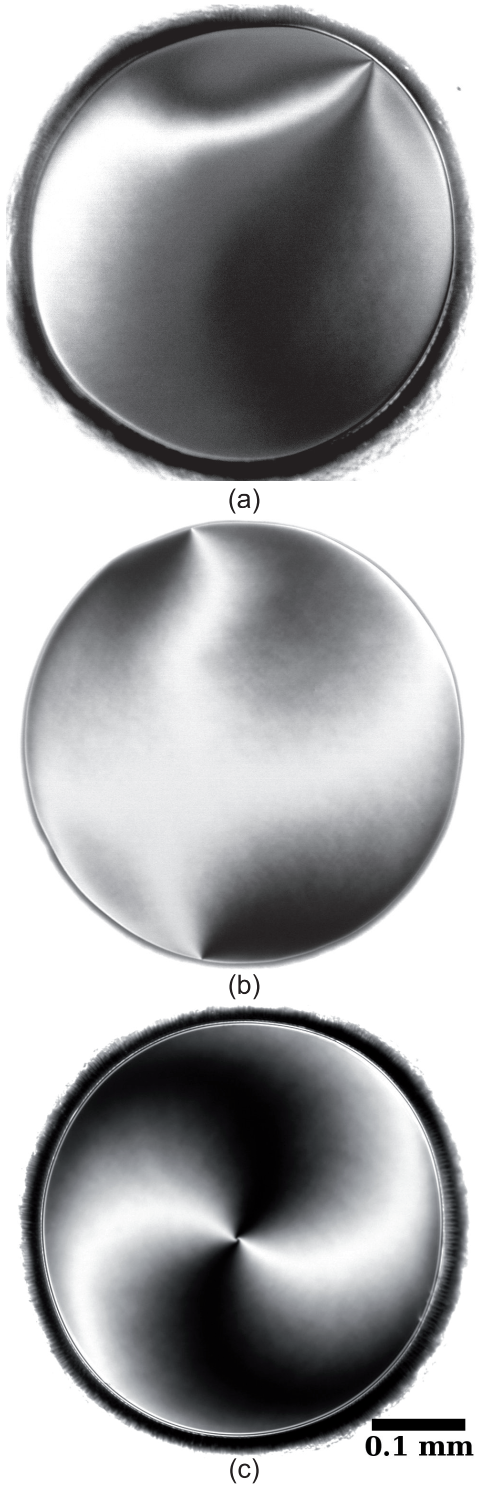

FIG. 6. The three configurations frequently encountered. (a) With a +1 defect at the edge of the film; (b) with two 1/2 defects at the edge of the film; (c) with a +1 defect in the center of the film. Photos taken between polarizer and analyzer slightly uncrossed.

perpendicular to the $\vec{c}$ director [39,40], the latter orients perpendicularly to the electric field. These measurements allowed us to calibrate the reflected intensity $I(\phi)$ (Fig. 5) making it possible the determination of the orientation of the molecules on the images.

In particular, we observed that the $\vec{c}$ director aligns parallel to the meniscus. This anchoring condition is incompatible with a director field uniformly aligned and shows us that the film always contains a +1 defect or several defects whose total topological rank is equal to +1. In practice, the defects are often localized on the edge of the meniscus as can be seen in Fig. 6(a) where a single +1 defect is present or in Fig. 6(b) where two +1/2 defects diametrically opposed are visible.

More rarely, the +1 defect detaches from the edge of the meniscus. In this case, the defect is placed in the center of the film when it is at rest, which minimizes the elastic energy of the system [Fig. 6(c)]. In this paper, we will only study the film behavior when the defect is attached to the meniscus and cannot move, which happens when it is pinned on a dust particle. The last important parameter is the film thickness, which can vary greatly depending on how the film is stretched. As the film properties, and the Leslie effect, in particular, are strongly dependent on it, this quantity must be measured accurately. The simplest method is to measure the film reflectivity under the microscope without polarizers. The reflectivity of the film reads

$$R(\lambda) = \frac{I_r(\lambda)}{I_i(\lambda)} = \frac{\sin^2 \mathcal{H}}{E + \sin^2 \mathcal{H}}, \tag{3}$$

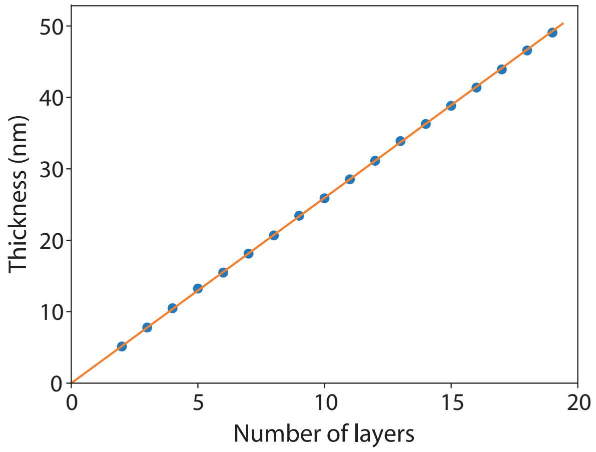

FIG. 7. Film thickness as a function of the number of layers.

where I_i is the incident intensity, I_r the reflected intensity and

$$\mathcal{H} = \frac{2\pi nH}{\lambda} \quad \text{and} \quad E = \frac{4n^2}{(n^2-1)^2}, \tag{4}$$

with $n(\lambda)$ the average refractive index of the LC, H the film thickness, and λ the light wavelength in vacuum. To measure the index dispersion, we measured with a motorized Jobin Yvon monochromator the reflectivity curves $R(\lambda)$ of several thick films and we fitted them with Eq. (3) by assuming that the optical index was given by a simplified Cauchy law:

$$n(\lambda) = A + \frac{B}{\lambda^2}. \tag{5}$$

From these fits with three parameters (H, A, B), we obtained

$$A = 1.503 \pm 0.005 \quad \text{and} \quad B = 6500 \pm 100\,\text{nm}^2. \tag{6}$$

We then measured the thickness of a large number of films. Assuming that each film has a thickness multiple of the layer thickness, we obtained the graph of Fig. 7, from which we deduced the layer thickness at 25 °C: 2.60 nm.

These data being known, we then plotted in Fig. 8 the film reflectivity as a function of the film thickness given in number of layers at the two wavelengths $\lambda = 436$ nm and $\lambda = 546$ nm. These two wavelengths correspond to two intense lines of the mercury vapor lamp used in our experiments to observe the films. This graph shows that measuring the reflectivity of a film at these two wavelengths is now enough to measure its thickness without ambiguity. This simplified procedure was used to measure the film thickness in all of our experiments.

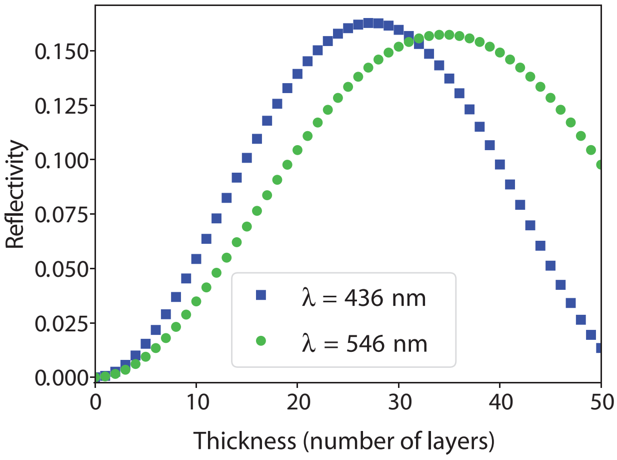

FIG. 8. Film reflectivity as a function of its thickness given in number of layers for two different wavelengths.

III. EXPERIMENTAL RESULTS

In this section, we separately describe the problem of phase winding when a flow of ethanol is established and that of phase unwinding when this flow is stopped.

A. Phase winding and target formation

In this section we describe the behavior of a film of uniform thickness when it is subjected to a flow of ethanol. The control parameters are the film thickness and the percentage of ethanol vapor or, equivalently, the difference in ethanol vapor pressure $\Delta\mathcal{P}$ across the film given by Eq. (2). In all the experiments reported here, the defect is trapped on the meniscus and immobile.

1. Transient regime

The first thing to notice when a film initially at rest is subjected to a flow of ethanol is a rotation of the molecules. This is particularly visible in the center of the film between slightly uncrossed polarizers where the reflected intensity begins to vary periodically over time. This rotation is rapidly accompanied by the formation of a target-shaped pattern as can be seen in the sequence of snapshots shown in Fig. 9 and in the Supplemental Movie SM1 [41].

The second observation is the presence of significant flows in the film, visible to naked eye, with velocities that can be as large as 2 mm/s for a percentage of ethanol vapor of 50% [42]. These flows arise everywhere in the film, and even before the rotation of the molecules begins. They are shown by the red arrows in Fig. 9. As we have already said above, but it is worth repeating here, these flows are not due to an artefact, i.e., to air flows on either side of the film, but to the presence of a flow of ethanol to which is associated a chemohydrodynamical Leslie effect. This can be checked immediately since the flows and the rotation of the director stop almost instantaneously when the flow of air with ethanol is replaced by a flow of dry air with the same rate of flow. It must be noted that these flows strongly influence the rotation of the director, in particular, near the edge of the film where they can prevent the rotation of the director, at least at the beginning of the winding process. This phenomenon is clearly visible in Fig. 9(f) where we can see that the bands do not reach the edge of the film. To characterize the transient regime, we measured the winding angle of the $\vec{c}$ director in the center of the film as a function of time for the film of Fig. 9. The corresponding curve for a percentage of ethanol vapor of 50% is shown in Fig. 10. This curve shows that ϕ increases, meaning that the $\vec{c}$ director rotates counterclockwise when the flow of ethanol vapor is directed upwards. We also see that the rotation velocity was maximum at the beginning and remained constant as long as the number of revolutions of the director was small, typically less than 5. This means that, in this regime, the elasticity is

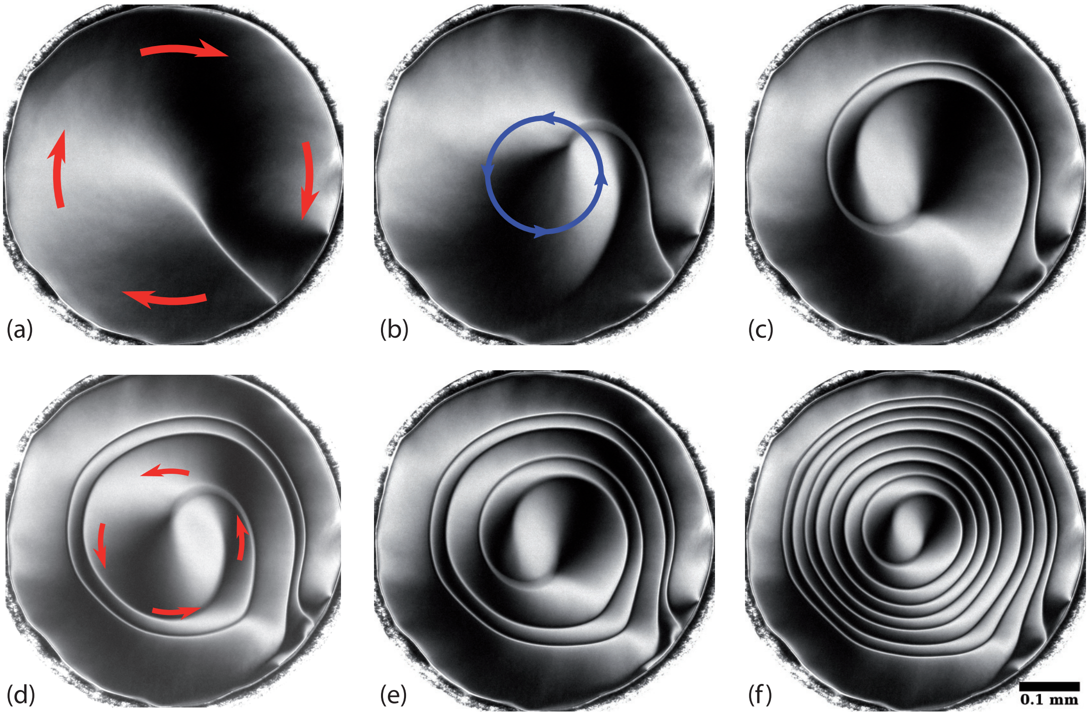

FIG. 9. Sequence of snapshots showing the winding of the $\vec{c}$ director under a flow of ethanol. At time $t = 0$ a 50% ethanol flow is imposed to the film; (a) $t = 9$ s; (b) $t = 12.1$ s; (c) $t = 13.2$ s; (d) $t = 14.1$ s; (e) $t = 14.8$ s; (f) $t = 17.4$ s. The red arrows drawn on snapshots (a) and (d) show the direction of the flows. The blue arrows on snapshot (b) show the sense of rotation of the director. The film is 10 layers thick.

negligible, and that the Leslie torque generated by the flow of ethanol equilibrates with the viscous torque. We shall see in the theoretical section that the Leslie torque is proportional to $\Delta\mathcal{P}$ while the viscous torque is proportional to the rotation velocity of the director, provided that the flows can be neglected. As a consequence, the initial rotation frequency f should be proportional to $\Delta\mathcal{P}$ in first approximation. To check to what extent this prediction was verified, we measured f as a function of $\Delta\mathcal{P}$ in the same film. The result is shown in Fig. 11 for the film of Fig. 9. We see that the curve presents an affine behavior, but does not pass through the origin, because no winding was observed for a percentage of ethanol vapor lower than 15%. For these low vapor rates, the film remained in the configuration of Fig. 9(a). We did, however, observe flows inside near the edge of the film, which we believe probably

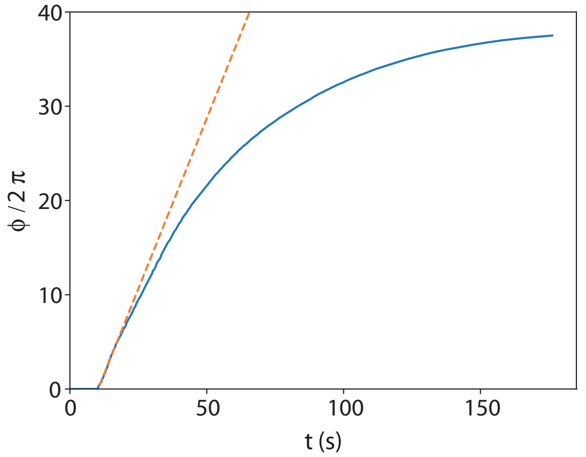

FIG. 10. Time course of the phase ϕ in the center of the film for a percentage of ethanol vapor of 50%. The slope of the dashed line gives the initial rotation frequency f. This curve has been obtained from the images shown in Fig. 9.

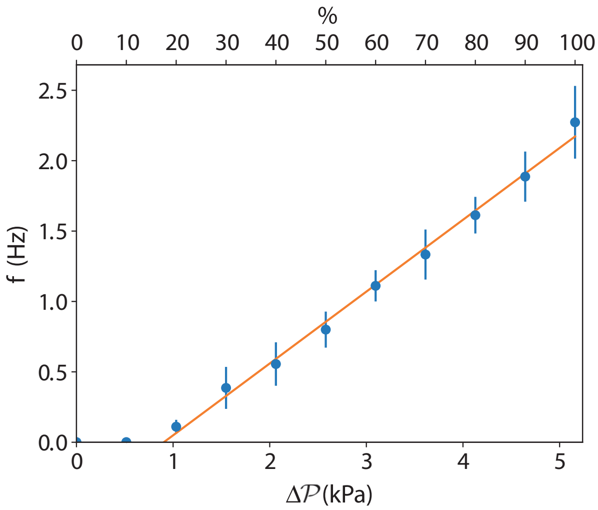

FIG. 11. Rotation frequency as a function of the percentage of ethanol vapor. These measurements have been performed at the beginning of the winding with the film shown in Fig. 9. The solid line is the best linear fit of the experimental points ignoring the first two. The error bars correspond to variations observed over several measurements.

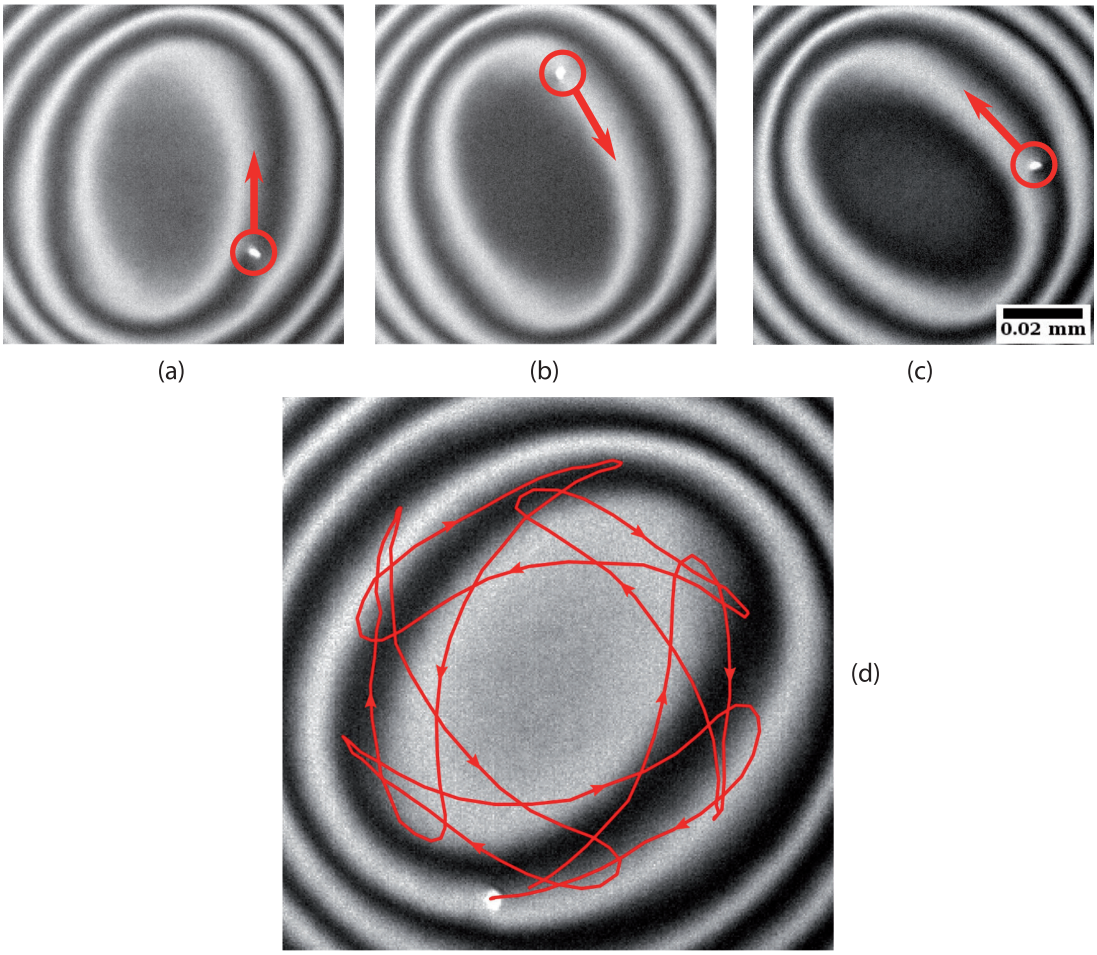

FIG. 12. Experimental evidence of a flow in the center of the target during the winding of the $\vec{c}$ director. (a–c) The circles and the arrows indicate the position and the direction of the particle at different times: (a) $t = 0$ s, (b) $t = 1.8$ s; (c) $t = 3.5$ s. The film is 10 layers thick and the percentage of ethanol vapor is 50%. (d) Trajectory followed by the particle during one turn (about 20 s here).

prevented the rotation of the director in the current configuration. Other configurations, with a $+1$ defect in the center of the film, in which flows are present while the director does not or very little winds, will be presented in a forthcoming paper.

These preliminary observations show that the flows play an important role in the freestanding films, at least at the beginning of the winding, contrary to what was observed in Langmuir monolayers [32].

We now return to the curve of Fig. 10. When the number of turns is larger than five, the rotation velocity starts to decrease. This is clearly due to an increase of the elastic torque when the turns accumulate. In this regime, the pattern looks more and more like a target between slightly uncrossed polarizers. But contrary to what is observed in Langmuir monolayers, the center of this target is not circular, but oval as can be seen in the photos of Fig. 12 taken during the transient regime. The question that then arises is to find the origin of this deformation. Is it due to elastic anisotropy or to the presence of flows?

To try to answer this question, we investigated whether there were still significant flows near the center of the target at this stage of the winding. For this purpose, we followed the trajectory of a dust particle which had accidentally fallen onto the film. This trajectory is shown in Fig. 12 and Supplemental Movie SM2 [41]. We see that the particle performs a back and forth movement in the central area while rotating globally in the same direction as the director in the center of the film. More precisely, during one turn, the particle goes back and forth three times and practically returns to its initial position. During this sequence, the observed maximum velocity of the particle is of the order of 0.02 mm/s and the director takes about 20 s to rotate by 2π. This observation shows that the flows in the center of the pattern are complex and not marginal at all. We now note that this trajectory cannot be explained solely by the *backflow* produced by the rotation of the director, because, in that case, we should only observe circular flows in the same direction as the winding. This observation suggests that the chemohydrodynamic Leslie force must be largely responsible for these flows and probably responsible for the deformation of the target. This point will be confirmed later.

2. *Stationary regime*

At very long time (typically after a quarter of an hour), a stationary regime is reached. In this limit, the target remains unchanged under the microscope, meaning that the director stops to rotate. A typical target at equilibrium is

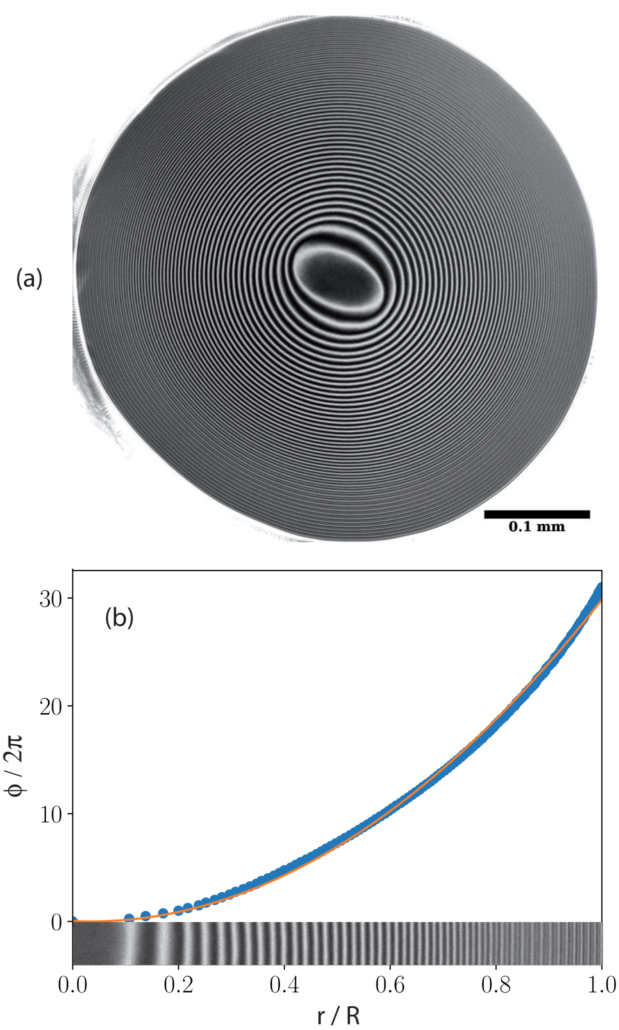

FIG. 13. Target pattern observed at equilibrium. The film is 10 layers thick. The percentage of ethanol vapor injected under the film is 50%. (b) Phase profile measured along a radius of this film. The solid red line is the best parabolic fit.

shown in Fig. 13(a). We note that its center is still deformed, which suggests that there are still flows in this steady state. In Fig. 13(b) we plotted the phase ϕ measured along a radius as a function of r/R where R is the film radius. This graph shows that the phase is well fitted with a parabolic law, as already observed in the Langmuir monolayers [32]. Figure 14 shows the equilibrium targets for various values of the percentage of ethanol vapor. This graph shows that the smaller the percentage, the less the target is wound. However, the center of the targets is always strongly deformed, which means that the flows play an important role whatever the percentage of ethanol vapor. Finally, we measured the number of turns at equilibrium $n_{\max} = \phi_{\max}/2\pi$. Figure 15 shows that $n_{\max}$ is proportional to $\Delta\mathcal{P}$ and Fig. 16 shows that it decreases when the film thickness increases at fixed $\Delta\mathcal{P}$ (corresponding here to a percentage of ethanol vapor of 50%). Such a behavior is expected as the flow of ethanol must decrease when the film thickness increases.

The dependence with the thickness is not trivial. Indeed one might expect $n_{\max}$ to vary as $1/H$ since $n_{\max}$ must be proportional to $\Delta\mathcal{P}/H$, by assuming that all the material constants integrated over the film thickness are just proportional to the film thickness. This dependence is not observed experimentally as shown by the $1/H$ curve plotted in Fig. 16. This means that the material constants integrated over the film thickness, and in particular the elastic constants, are probably not proportional to the film thickness. This interpretation is plausible because the films studied are very thin, with less

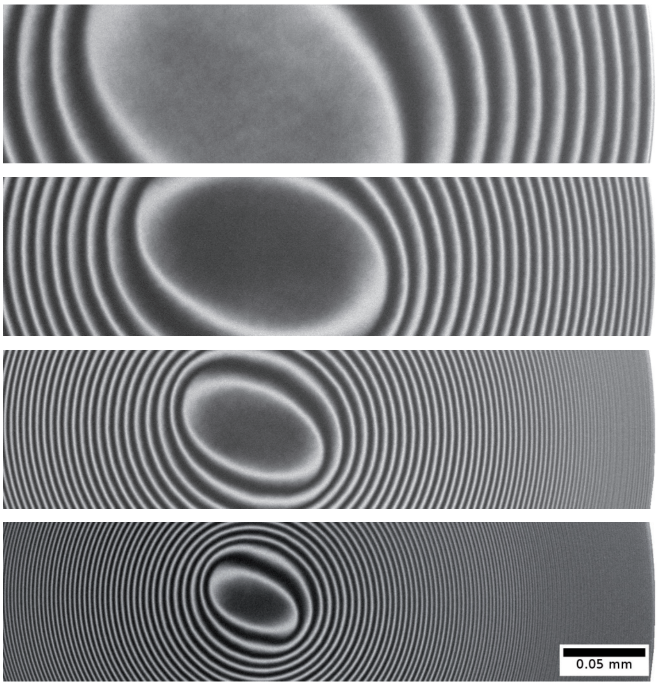

FIG. 14. Images of the target pattern obtained with different percentages of ethanol vapor. From top to bottom, the percentage is 10%, 20%, 50%, and 100%.

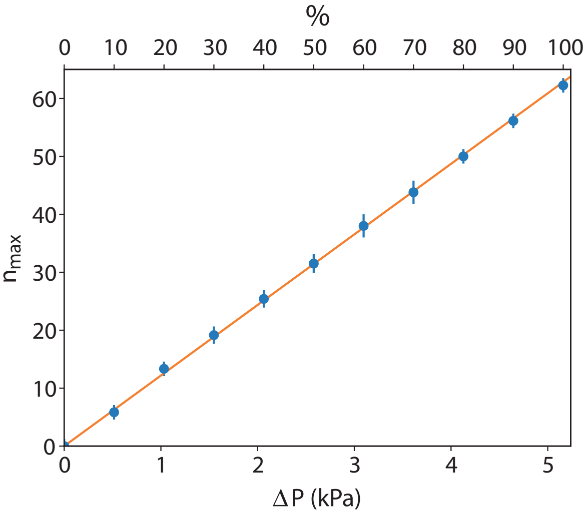

FIG. 15. Number of turns at equilibrium as a function of the percentage of ethanol vapor for the 10-layers-thick film of Fig. 13. The error bars correspond to the variations observed by making several measurements. The solid line corresponds to the best linear fit.

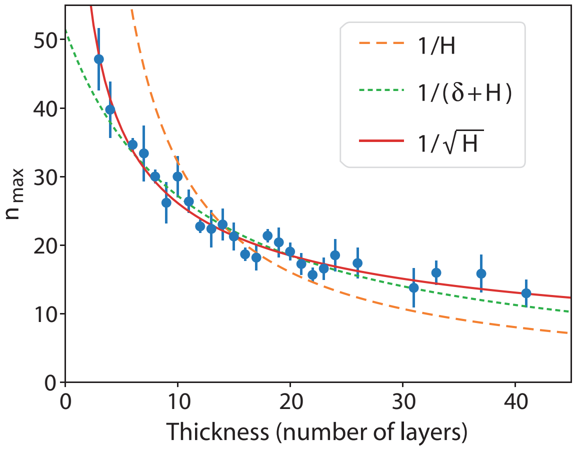

FIG. 16. Number of turns at equilibrium as a function of the film thickness for films of 0.5 mm in diameter. The percentage of ethanol vapor is 50%. The error bars have been calculated from the variations observed with different films. The lines correspond to the best fits with the functions given on the graph.

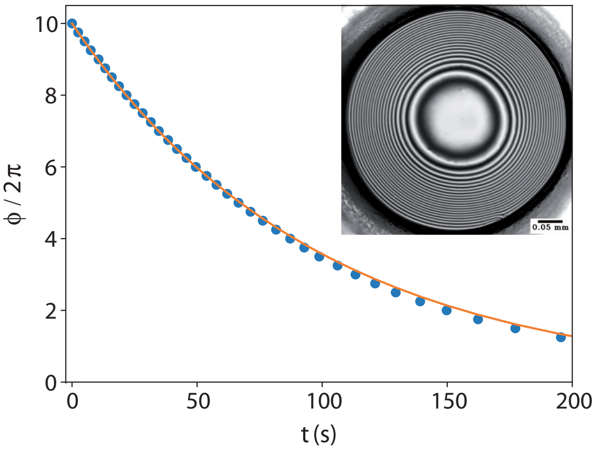

FIG. 17. Angle ϕ in the center of the film as a function of time measured during the phase unwinding when the flow of ethanol is cut off. The solid line is the best fit with an exponential law. The inset shows the target pattern observed during the phase unwinding. The film is 20 layers thick.

than 20 layers in general, meaning that the surface effects are certainly important as already noted by several authors in other materials (for a review, see Ref. [39]). Another complication could come from the formation of a thin boundary layer of thickness δ in the vicinity of the film in which the concentration of ethanol changes. In that case, a simple calculation shows that $n_{\max}$ must vary as $1/(H+\delta)$ by assuming that the material constants are proportional to the film thickness. The details of the model are given in Ref. [43]. The best fit of the experimental data with this law leads to $\delta = 29$ nm, but the fit is not yet perfect as can be seen in Fig. 16. In practice, all these effects must act at the same time, and it would be necessary to measure all the material constants as a function of the film thickness to be able to disentangle them. This is an enormous task that goes well beyond the scope of this study. Note in passing that a best fit was obtained with a power law in $1/H^n$ with $n \approx 1/2$ as can be seen in Fig. 16, but we have no model to explain this dependence. We finally add to conclude that the defect sometimes detaches from the meniscus, in particular, at large percentage of ethanol vapor, and starts moving along the edge of the film. In that case, a new stationary regime is reached when the defect and the director rotate at the same angular velocity. An example is shown in Supplemental Movie SM3 [41]. In this regime, the final number of turns is always less than that reached when the defect is fixed, but it can vary from one experiment to another because it depends on the mobility of the defect in the vicinity of the meniscus. For this reason we did not study this regime in detail.

B. Phase unwinding

If the flow of ethanol is stopped and replaced by a flow of dry air once the target is formed, then the latter unwinds to relax the elastic energy it has stored. In practice, it is also possible to prepare a target by blowing air on the film with a small fan or by using a rotating electric field. After stopping the fan or the electric field, the target unwinds in the same way as when stopping the flow of ethanol. In all the cases, the only forces involved during the unwinding are the elastic and viscous forces. We observed that at the start of the unwinding, the relaxation was not exponential and depended on the way the target had been wound. For this reason, we did not study this initial regime in detail. By contrast, we observed that after a few turns, the unwinding process was always the same, and no longer depended on the initial conditions. More precisely we observed that the phase ϕ measured in the center of the film relaxed exponentially over time as can be seen in Fig. 17 and Supplemental Movie SM4 [41]. We also observed that in this regime, the center of the target was much less deformed than during the winding process in the presence of the ethanol flow. This can be seen by comparing the targets in Figs. 14 and 17. This observation is important because it seems to show that it is indeed the flows created by the Leslie force, and not the elastic anisotropy, that are responsible for the oval deformation of the target in the center of the film. This interpretation will be confirmed later by our numerical simulations. We also observed by following under the microscope the movement of small smoke particles deposited on the film, that there were *backflow* effects inside the film. The orthoradial velocity profile normalized with the number of turns measured in the center of the film is shown in Fig. 18(a). This graph shows that this ratio is constant over time, which indicates that the velocity decreases with the same exponential law as the phase as a function of time. We also show in Fig. 18(b) how the maximum velocity measured in the film decreases (in absolute value) as a function of time. This value is reached at a distance of the order of $0.6R$ from the center of the film, by denoting by R the radius of the film. As expected, this curve is well fitted by an exponential law with the same characteristic time as for the phase measured at the center of the film. For the 20-layers film shown in Fig. 17 the half-unwinding time $\tau_{1/2}$ is of the order of 67 s and the maximum velocity measured when the number of turns is equal to 10 is -0.06 mm/s.

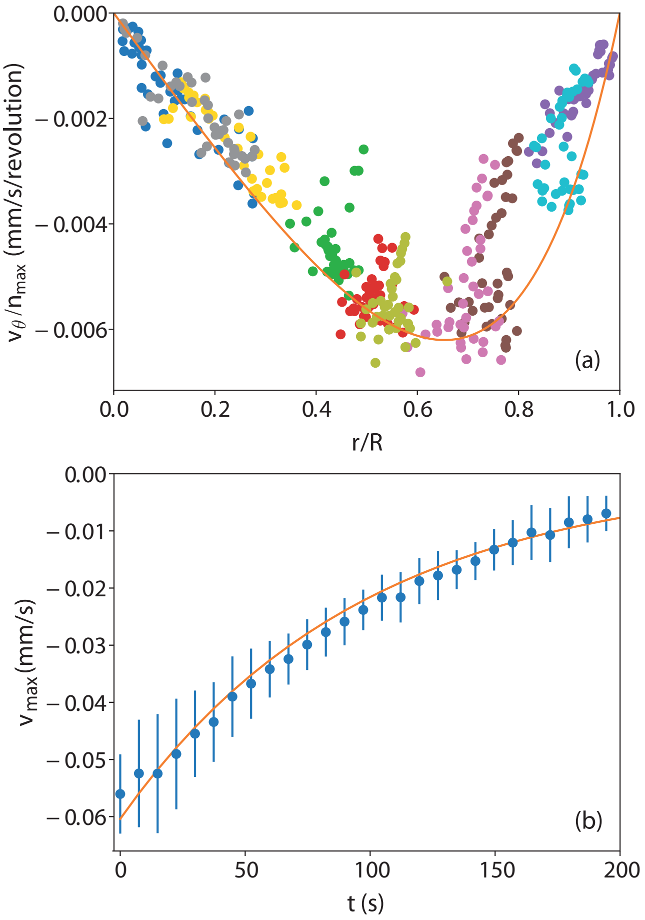

FIG. 18. (a) Velocity profile measured along a radius during the phase unwinding. Each color corresponds to a different tracer. For each tracer, the different points with the same color correspond to different times. The solid line is a fit with a law in $r - r^3$. (b) Maximal velocity as a function of time measured during the phase unwinding and its fit with an exponential law.

IV. THEORETICAL SECTION

In this section, we will begin by recalling the fundamental equations that govern the dynamics of freestanding films in the presence of a chemical Leslie effect. Then we will see how to solve them, first in the case of the winding in the presence of a vapor flow, and second in the case of the unwinding when the flow is removed. In each case, we will treat the problem first in a simplified way by neglecting the elastic anisotropy and the flows, and then in a more complete way by taking into account either the elastic anisotropy or the flows.

A. Governing equations

The hydrodynamic variables are the $\vec{c}$ director defined by the angle ϕ it makes with the x axis, the velocity $\vec{v}$ and the pressure P in the film. As the films are always very thin, we will assume that these quantities are homogeneous in the film thickness and only depend on the (x, y) coordinates.

The two equations which govern the dynamics of a film are the torque equation and the Cauchy equation. The first one mainly governs the rotation of the director while the second allows one to calculate the velocity. These two equations are nevertheless coupled and strongly nonlinear, which makes the problem difficult to solve.

Formally, the torque equation reads

$$\vec{\Gamma}^E + \vec{\Gamma}^V + \vec{\Gamma}^{\mathrm{cm}} = 0, \tag{7}$$

and the Cauchy equation reads

$$\vec{\nabla} \cdot \underline{\sigma}^V + \vec{\nabla} \cdot \underline{\sigma}^E + \vec{\nabla} \cdot \underline{\sigma}^{\mathrm{ch}} - \vec{\nabla} P = \vec{0}. \tag{8}$$

In these equations, $\vec{\Gamma}^E$, $\vec{\Gamma}^V$, and $\vec{\Gamma}^{\mathrm{cm}}$ are the elastic, viscous, and chimiomechanical components of the torque acting on the $\vec{c}$ director and $\underline{\sigma}^V$, $\underline{\sigma}^E$, and $\underline{\sigma}^{\mathrm{ch}}$ are the elastic, viscous, and chimiohydrodynamical components of the stress tensor. As for P, it is the pressure in the film given by the incompressibility condition

$$\vec{\nabla} \cdot \vec{v} = 0. \tag{9}$$

Note that we neglected the inertial term in the Cauchy equation because the Reynolds number in our experiments is always small with respect to 1, of the order of 10^{-3}–10^{-2}.

We now give the expression of these different torques and stresses as a function of the constants of the material.

The elastic torque and the elastic stress are equilibrium quantities which derive directly from the expression of the elastic free energy of deformation of the director field $\vec{c}$. For a film whose the thickness is very small compared to the helical pitch of the smectic-$C^\star$, the elastic energy is reduced to the following expression:

$$f[\vec{c}] = \tfrac{1}{2} K_S \big(\vec{\nabla} \cdot \vec{c}\big)^2 + \tfrac{1}{2} K_B \big(\vec{\nabla} \times \vec{c}\big)^2. \tag{10}$$

In this expression, K_S is the splay constant and K_B is the bend constant. Note here that K_B is renormalized by the presence of the polarization charges since the Smectic C* phase is ferroelectric [44–46]. For this reason, one may expect that K_B is larger than K_S in our films since the LC FELIX used in our experiments has a large spontaneous polarization (of the order of 20 nC/cm^2 according to Ref. [47]). In practice, we can split the elastic energy into two parts: an isotropic part that reads as a function of ϕ:

$$f^i[\phi] = \tfrac{1}{2} K (\vec{\nabla} \phi)^2, \tag{11}$$

and an anisotropic part, of expression:

$$f^a[\phi] = \tfrac{1}{2} K \epsilon \big[\cos(2\phi)\big(\phi_{,x}^2 - \phi_{,y}^2\big) + 2 \sin(2\phi) \phi_{,x} \phi_{,y}\big]. \tag{12}$$

In these equations, $K = \frac{K_S + K_B}{2}$ is the average elastic constant and $\varepsilon = \frac{K_B - K_S}{K_B + K_S}$ is a dimensionless coefficient that characterizes the elastic anisotropy. From these equations the elastic torque and the elastic stress can be calculated. For simplicity, we only give here their expressions in the case of isotropic elasticity when $\varepsilon = 0$:

$$\vec{\Gamma}^E = K \nabla^2 \phi \, \vec{k}, \tag{13}$$

where $\vec{k}$ is the unit vector normal to the film directed upwards, and

$$\underline{\sigma}^E = -K \begin{pmatrix} \phi_{,x}^2 & \phi_{,x}\phi_{,y} \\ \phi_{,x}\phi_{,y} & \phi_{,y}^2 \end{pmatrix} \tag{14}$$

in cartesian coordinates (x, y).

In a smectic-$C^\star$ film, the most general form of the nonequilibrium viscous stress tensor reads [48]:

$$\begin{aligned}\sigma_{ij}^V &= \mu_0 A_{ij} + \mu_3 (c_k A_{kl} c_l) c_i c_j + \lambda_2 (c_i C_j + c_j C_i)\\ &\quad + \lambda_5 (c_i C_j - c_j C_i) + \mu_4 (c_i c_k A_{kj} + c_j c_k A_{ki})\\ &\quad + \lambda_2 (c_i c_k A_{kj} - c_j c_k A_{ki}).\end{aligned} \tag{15}$$

In this expression, $\vec{C}$ is the corotational time derivative of the $\vec{c}$ director with respect to time:

$$\vec{C} = \frac{D\vec{c}}{Dt} - \vec{\Omega} \times \vec{c}, \tag{16}$$

where D/Dt denotes the total derivative with respect to time, $\vec{\Omega} = \frac{1}{2}\vec{\nabla} \times \vec{v}$ and A_{ij} is the strain rate tensor:

$$A_{ij} = \frac{1}{2}\left(\frac{\partial v_i}{\partial x_j} + \frac{\partial v_j}{\partial x_i}\right). \tag{17}$$

In practice, this tensor can be rewritten as in the nematic phase in the form:

$$\begin{aligned}\sigma_{i,j}^V &= \alpha_4 A_{i,j} + \alpha_1 (c_k A_{k,l} c_l) c_i c_j + \alpha_2\, c_j C_i + \alpha_3\, c_i C_j\\ &\quad + \alpha_5\, c_j c_k A_{k,i} + \alpha_6\, c_i c_k A_{k,j},\end{aligned} \tag{18}$$

with the correspondence:

$$\begin{aligned}\alpha_1 &= \mu_3\\ \alpha_2 &= \lambda_2 - \lambda_5\\ \alpha_3 &= \lambda_2 + \lambda_5\\ \alpha_4 &= \mu_0\\ \alpha_5 &= \mu_4 - \lambda_2\\ \alpha_6 &= \mu_4 + \lambda_2.\end{aligned} \tag{19}$$

We will use this form in the following. Note that, as in nematics, the viscosity coefficients must satisfy the Parodi relation [49]

$$\alpha_2 + \alpha_3 = \alpha_6 - \alpha_5. \tag{20}$$

From this expression, the nonequilibrium viscous torque can be calculated by using the relation $\Gamma_i^V = -\varepsilon_{ijk}\sigma_{jk}^V$ where ε_{ijk} is the Levi-Civita tensor. The calculation gives as in nematics

$$\vec{\Gamma}^V = -\gamma_1\, \vec{c} \times \vec{C} - \gamma_2\, \vec{c} \times \underline{A}\vec{c}, \tag{21}$$

where $\gamma_1 = \alpha_3 - \alpha_2$ and $\gamma_2 = \alpha_3 + \alpha_2 = \alpha_6 - \alpha_5$ are the two rotational viscosities of the phase. In cartesian coordinates, this torque reads $\vec{\Gamma}^V = \Gamma^V \vec{k}$ with

$$\begin{aligned}\Gamma^V &= -\gamma_1\left[\frac{D\phi}{Dt} + \frac{1}{2}(u_{,y} - v_{,x})\right]\\ &\quad - \frac{\gamma_2}{2}[\cos(2\phi)(u_{,y} + v_{,x}) + \sin(2\phi)(v_{,y} - u_{,x})]\end{aligned} \tag{22}$$

by denoting by u and v the two components v_x and v_y of the velocity and their derivatives with respect to x or y by a subscript x or y after a comma. In the presence of a gradient of chemical potential, which is caused in our experiments by the flow of ethanol, new terms appear in the expressions of the nonequilibrium torque and the stress tensor. These terms have been calculated for the first time by Leslie in cholesterics in the presence of a thermal gradient [3], but they also exist in the smectic-$C^\star$ phase because of its chirality and the absence of mirror symmetries. A complete derivation of these terms in the simplified case of a smectic-$C^\star$ film, using a generalization of the Akopyan and Zel'dovich method [50,51], can be found in Refs. [43,52]. When the flow of particles is normal to the film, this calculation shows the existence of a new nonequilibrium chemomechanical torque of expression

$$\vec{\Gamma}^{\mathrm{cm}} = \nu\, \Delta\mathcal{P}\, \vec{k}, \tag{23}$$

and of a new nonequilibrium chemohydrodynamical stress of expression

$$\underline{\sigma}^{\mathrm{ch}} = \frac{\mu\Delta\mathcal{P}}{2}([\vec{c} \times \vec{k}] \otimes \vec{c} + \vec{c} \otimes [\vec{c} \times \vec{k}]), \tag{24}$$

where the symbol $\otimes$ denotes the dyadic product between two vectors $[(\vec{a} \otimes \vec{b})_{ij} = a_i b_j]$. Here, $\Delta\mathcal{P}$ is the difference in vapor pressure between the bottom and the top of the film. In cartesian coordinates (x, y) this stress reads

$$\underline{\sigma}^{\mathrm{ch}} = \frac{\mu\Delta\mathcal{P}}{2}\begin{pmatrix}\sin(2\phi) & -\cos(2\phi)\\ -\cos(2\phi) & -\sin(2\phi)\end{pmatrix}. \tag{25}$$

Note that a nonequilibrium chemomechanical stress of components $\sigma_{ij}^{\mathrm{cm}} = -\varepsilon_{ijk}\Gamma_k^{\mathrm{cm}}$ is associated with the chemomechanical torque (23). As this stress has zero divergence, it does not enter into the Cauchy equation and so it will not play any role in our study, knowing that we will fix angle (or phase) ϕ at the edge of the film in all of our calculations.

In the following, we solve these equations first in the winding case and then in the unwinding case. Each time, we will proceed in a progressive way, by first analyzing the solution when the elastic anisotropy and the flows are neglected. We will then analyze separately the role of elastic anisotropy and of flows.

B. Phase winding

1. Analytical solution in isotropic elasticity and in the absence of flow

Phase dynamics is particularly simple to analyze when the elastic anisotropy and the flows are neglected ($\varepsilon = 0$ and $\vec{v} = 0$). In that case the equations reduce to the torque equation of simplified form:

$$\gamma_1 \frac{\partial\phi}{\partial t} = K\nabla^2\phi + \nu\Delta\mathcal{P}. \tag{26}$$

This equation was already used to study the phase winding in Langmuir monolayers [32]. It shows that, at the beginning, when the flow of ethanol is switched on, the phase uniformly winds as

$$\phi(\vec{r}, t) = 2\pi f t, \tag{27}$$

with an initial rotation frequency f given by

$$f = \frac{\nu\Delta\mathcal{P}}{2\pi\gamma_1}. \tag{28}$$

This formula shows that f is proportional to $\Delta\mathcal{P}$. It is important to note here that this formula remains valid in the presence of a defect since Eq. (26) is linear. It is indeed possible to add to solution (27) the stationary solution to equation $\Delta\phi = 0$ corresponding to the defect. In practice, this behavior is not strictly observed experimentally (see Fig. 11) because of the complications coming from the flows and the elastic anisotropy. This law must also rapidly fail because the director cannot rotate on the edge of the film. By assuming that $\phi = 0$ at the edge of the film [53], this condition leads to an equilibrium target pattern at time $t \to \infty$ when $\partial\phi/\partial t = 0$ given by

$$\phi(\vec{r}, t \to \infty) = 2\pi n\left[1 - \left(\frac{r}{R}\right)^2\right], \tag{29}$$

where we have set

$$n = \frac{\nu \Delta\mathcal{P} R^2}{8\pi K}. \tag{30}$$

Here, r is the polar coordinate by taken the origin in the center of the film and R is the film radius and n represents the number of turns at equilibrium. This quantity will be chosen as the control parameter in the following, instead of $\Delta\mathcal{P}$. This law shows that, at equilibrium, the phase profile along a radius is parabolic. This dependence is again pretty well observed experimentally as shown in Fig. 13.

In the intermediate regime, Eq. (26) must be solved with all the terms. With the boundary conditions $\phi(\vec{r}, 0) = 0$ and $\phi(R, t) = 0$, this equation has a solution that can be expressed using Bessel functions. We show the results graphically in Fig. 19.

2. *Numerical solution in anisotropic elasticity and in the absence of flow*

The previous calculation leads to perfectly circular targets. However, experimentally, targets are deformed in the center not only during the transient regime, but also in the stationary regime, as can be seen in Figs. 12–14. In this paragraph, we analyze which role plays the elastic anisotropy in the deformation of the targets when the flows are negligible.

This problem is unfortunately much more complex than in the isotropic case. To solve it, we could have solved the torque equation in anisotropic elasticity, but this is difficult because ϕ now depends not only on r but also on the polar angle θ. For this reason, we adopted another strategy consisting in minimizing an effective energy.

To find this energy, let us return to the torque equation of general expression when $\vec{v} = 0$:

$$\gamma_1 \frac{\partial\phi}{\partial t} = \Gamma^E + \nu\Delta\mathcal{P}. \tag{31}$$

In this equation $\Gamma^E = \delta f/\delta\phi$ is the elastic torque calculated by taking $f[\phi] = f^i[\phi] + f^a[\phi]$ where $f^i[\phi]$ and $f^i[\phi]$ are given by Eqs. (11) and (12).

By setting $\phi(t) = \phi_t$ and $\phi(t + \delta t) = \phi$, and by approximating Eq. (31) by an implicit Newton type scheme,

$$\frac{\partial\phi}{\partial t} \simeq \frac{\phi - \phi_t}{\delta t}, \tag{32}$$

it is possible to create two new functionals corresponding respectively to the temporal term,

$$t[\phi, \phi_t] = \frac{\gamma_1}{2\delta t}(\phi - \phi_t)^2, \tag{33}$$

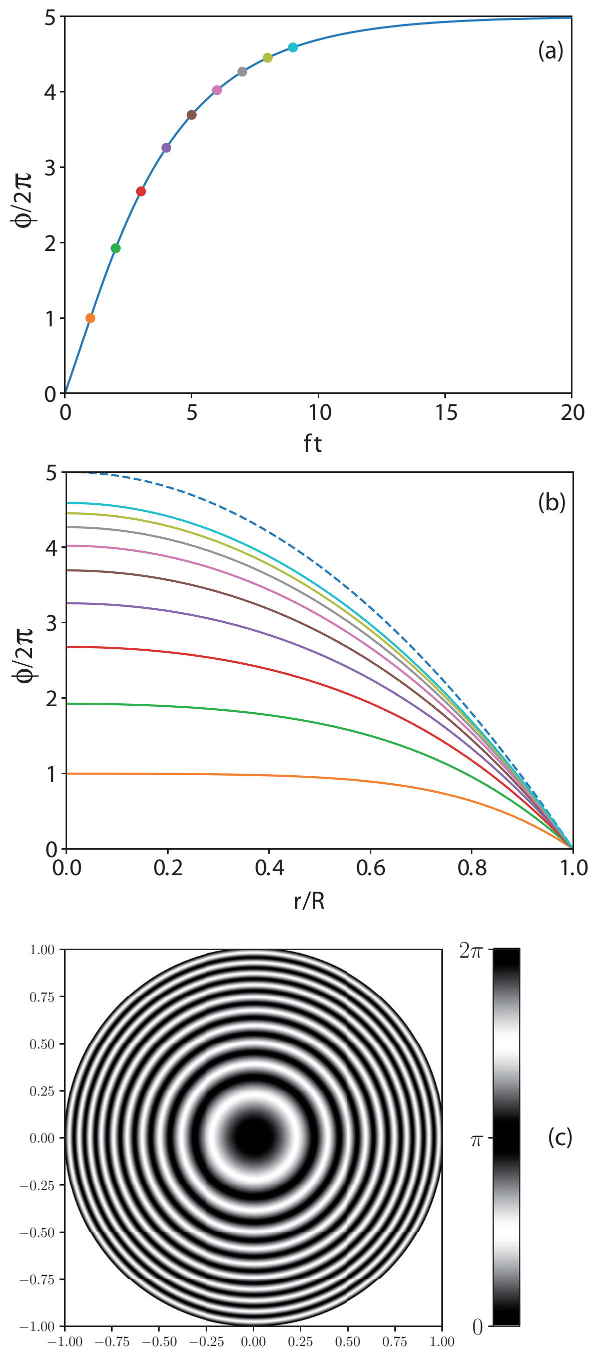

FIG. 19. Solution of Eq. (26) for a final winding of five turns. (a) Winding angle in the center as a function of time scaled using $1/f$ as the characteristic time. (b) Radial angle profiles at different times. Each colored curve corresponds to a point of the same color in panel (a). The dashed curve corresponds to the equilibrium curve obtained when $t \to \infty$. (c) Aspect of the target between slightly uncrossed polarizers when $n = 5$. The local intensity is calculated by taking $I = \sin^2\phi$.

and to the Leslie term,

$$l[\phi] = -\nu G\phi, \tag{34}$$

the derivative with respect to ϕ of which gives back the associated torques. The torque equation can then be rewritten in the form

$$\frac{\delta e}{\delta \phi} = 0, \tag{35}$$

where $e[\phi]$ is an effective energy of the form

$$e[\phi, \phi_t] = t[\phi, \phi_t] + l[\phi] + f^i[\phi] + f^a[\phi]. \tag{36}$$

In the following, we will take R as a unit length and $\tau = R^2/D$ as a unit of time, where $D = K/\gamma_1$ is the average orientational diffusion coefficient. All our calculations will be made using dimensionless variables:

$$\begin{aligned} \tilde{x} &= \frac{x}{R},\ \ \tilde{y} = \frac{y}{R} \\ \tilde{v} &= \frac{R}{D} v \\ \tilde{P} &= \frac{R^2}{K} P \end{aligned} \tag{37}$$

and we will set

$$a_i = \frac{\alpha_i}{\gamma_1} \text{ and } X = \frac{\mu}{\nu}. \tag{38}$$

With these variables, the effective energy is written in the dimensionless form as follows:

$$\begin{aligned} \tilde{e}[\phi, \phi_t] = {} & \tfrac{1}{2\tilde{\delta t}}(\phi - \phi_t)^2 - 8\pi n\phi + \tfrac{1}{2}\left(\phi_{,\tilde{x}}^2 + \phi_{,\tilde{y}}^2\right) \\ & + \tfrac{1}{2}\epsilon\left[\cos(2\phi)\left(\phi_{,\tilde{x}}^2 - \phi_{,\tilde{y}}^2\right) + 2\sin(2\phi)\phi_{,\tilde{x}}\phi_{,\tilde{y}}\right], \end{aligned} \tag{39}$$

where n is defined in Eq. (30) and corresponds to the numbers of turns at equilibrium calculated by neglecting the anisotropy and the flows.

The next step to solve the torque equation for each time step was to minimize this functional with respect to $\phi = \phi(t + \delta t)$ knowing $\phi_t = \phi(t)$. In addition, it was possible to directly calculate the final equilibrium state by just omitting the time term in this equation.

From a practical point of view, the energy functional was developed on a Finite Element space using the C++ library deal.II [54]. This energy was then minimized thanks to a confidence region algorithm ensuring both a global and rapid convergence towards the minimum energy. All the details on this numerical method are given in Refs. [43,55]. It should just be noted that the main numerical limitations came from the execution time. Indeed, it was necessary to have a sufficiently fine grid to correctly describe the terms in $\cos(2\phi)$ and $\sin(2\phi)$ in the anisotropic part of the energy. In particular, the use of an adaptive grid could not help to solve this problem, because the gradients of ϕ are important everywhere in the film. To overcome this problem, we therefore limited ourselves to low winding simulations (n ranging from 2 to 20) and we worked with grids with the highest level of refinement possible. In practice, the equilibrium target calculations were made on a grid containing 5 million cells on which a revolution of the director is described by 200 points (for $n = 5$). The computation time necessary to solve the problem was typically 10 hours and increased up to one day for the largest values of the anisotropy. As for the dynamic calculations on the winding of a target, there were performed using a coarser grid (50 points per revolution for $n = 5$) so that each time step could be calculated over a duration of the order of a minute. Using this method, we calculated equilibrium targets for different values of the anisotropy. The result for $\varepsilon = 0.7$ ($K_B/K_S = 5.7$) and $\varepsilon = 0.95$ ($K_B/K_S = 39$) are shown in Fig. 20 when $n = 5$. These images show that the targets are little deformed in the center, even at very large anisotropy, and bear little resemblance to the targets observed experimentally (see Figs. 13 and 14). We also plotted in Fig. 21 the number of turns at equilibrium $n_{\max}$ divided by n as a function of the anisotropy. This number increases, but not so much, since we find $n_{\max} \approx 1.2\,n$ at $\varepsilon = 0.95$. We also studied the influence of the anisotropy on the phase winding process. The results are shown in Fig. 22 where we plotted the evolution of the angle measured in the film center scaled to its maximal value as a function of the dimensionless time for different values of the anisotropy. This graph shows that the curves are not very different. Additionally, we plotted the dimensionless half-winding time as a function of the anisotropy in Fig. 23. These two graphs show that the winding process slows down when the anisotropy increases, but this slowing down is not considerable, even at the strongest anisotropies.

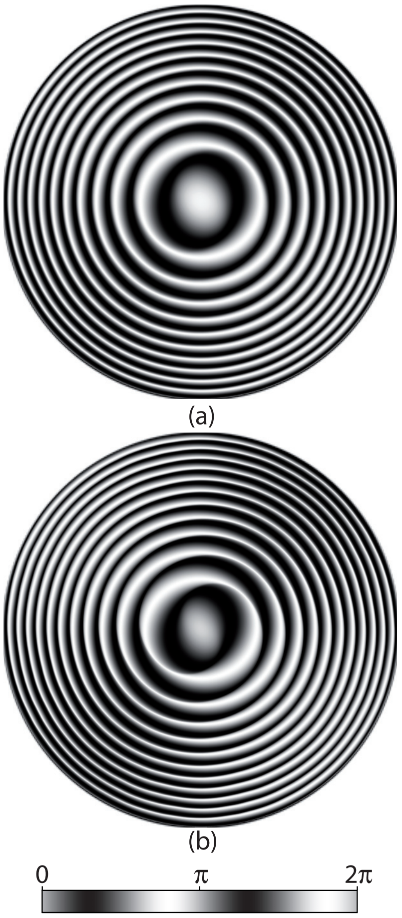

FIG. 20. Target pattern at equilibrium calculated for $n = 5$ and two different values of the elastic anisotropy: (a) $\varepsilon = 0.7$; (b) $\varepsilon = 0.95$.

All these results show that the elastic anisotropy is not so crucial in our system. In particular, it cannot alone explain the deformation of the targets in the center of the film during the

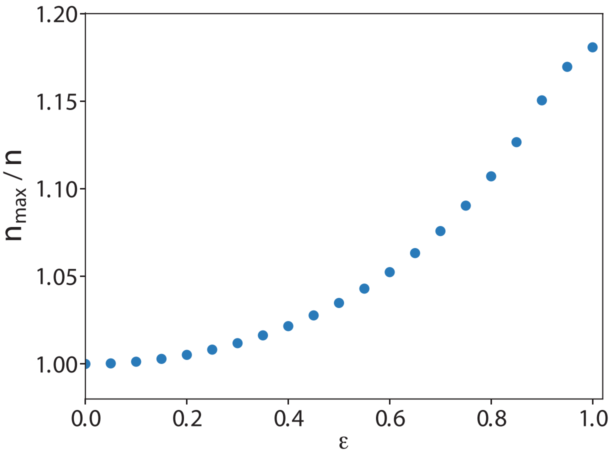

FIG. 21. Number of turns at equilibrium divided by n as a function of the elastic anisotropy when the flows are neglected. The curve has been plotted for $n = 5$ but it should be emphasized that this curve is almost independent of n.

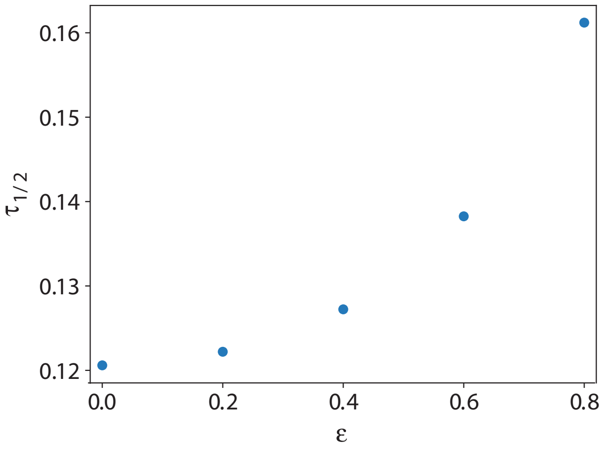

FIG. 23. Half-winding time as a function of the elastic anisotropy when the flows are neglected. These results have been obtained by taking $n = 5$ but it should be emphasized that they depend very little on this parameter.

winding. For this reason, and also to simplify the calculations, we neglected the elastic anisotropy in the study of flows that we present now.

3. Numerical solution in isotropic elasticity and in the presence of flow

In the presence of flows, the previous minimization method can no longer be used and it is necessary to directly solve the three fundamental equations of the dynamics, namely the torque equation (7), the Cauchy equation (8), and the incompressibility equation (9).

From a mathematical point of view, these equations resemble Boussinesq's equations which describe the flow of a fluid whose density varies with temperature. In our problem, the angle ϕ plays the same role as the temperature in the Boussinesq problem since the torque equation is a diffusion equation in which the Leslie forcing term is equivalent to a heating term in the heat equation. Our problem is nevertheless more complicated since it also involves two coupling terms between the director and the velocity proportional to γ_1 and γ_2 which are not present in the usual heat equation. As for our Cauchy equation, it is formally equivalent to the Stokes equation for the velocity in the Boussinesq problem, the Leslie chemohydrodynamical force and the elastic force replacing the buoyancy force in our case.

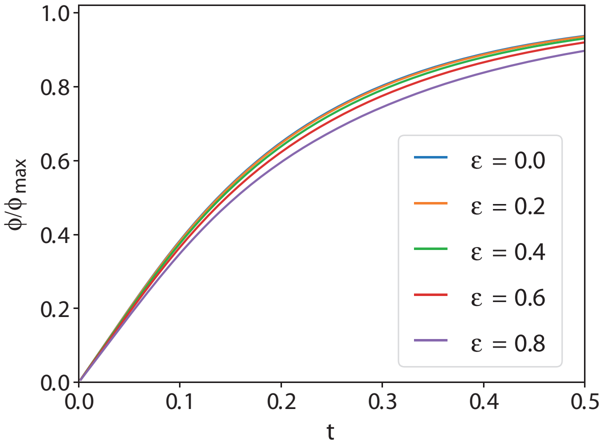

FIG. 22. Angle ϕ in the center of the film scaled by $\phi_{\max} = 2\pi n_{\max}$ as a function of the dimensionless time when the flows are neglected. Simulations were performed with $n = 5$ for different values of the elastic anisotropy ε. Angle $\phi_{\max}$ corresponds to the final value of ϕ during the winding. $n_{\max}$ is given in Fig. 21.

If this analogy seems a little artificial, it is nevertheless relevant from a numerical point of view. As for the Boussinesq system, we are dealing with two coupled fields $\phi(\vec{r}, t)$ and $\vec{v}(\vec{r}, t)$. The first, scalar, is governed by a diffusion equation. The second, vectorial, satisfies a Stokes type equation. For this reason, the same general techniques of resolution as in the Boussinesq problem can be used here.

In particular, the fact of neglecting the inertial term in the Cauchy equation makes it possible to treat it separately from the torque equation. In other words, the absence of the inertial term in the Cauchy equation implies that to a given orientation field $\phi(\vec{r}, t)$ is associated a single velocity field $\vec{v}(\vec{r}, t)$. A method to solve a time step is therefore to solve successively and independently these two equations.

In practice, we will use the velocity field of the previous time step to solve the torque equation with ϕ as the only unknown. In this way, a new estimate of ϕ is obtained, which can be used in the Cauchy equation to calculate a new, more precise estimate of $\vec{v}$. Repeating this process allows one to refine the general solution $(\phi, \vec{v})$ until it satisfies the two equations.

The analogy with the Boussinesq problem also allowed us to simply answer complicated numerical questions. In particular, it is well known that the choice of the finite element space is crucial to correctly solve the Stokes equation. Using a pair of unstable spaces for the velocities and the pressure will result in a potentially false and nonphysical solution. In our case, and by analogy with other similar numerical problems [56], we used the mixed space $Q_2^2 \times Q_1$, that was proven to be stable for solving the Stokes equation.

In practice, our equations were made dimensionless before to be solved numerically. With the variables given in Eq. (37), the torque and Cauchy equations are written in dimensionless form as

$$\frac{D\phi}{D\tilde{t}} = \tilde{\Delta}\phi + 8\pi n - \frac{1}{2}(\tilde{u}_{,\tilde{y}} - \tilde{v}_{,\tilde{x}}) - \frac{\gamma}{2}[\cos(2\phi)(\tilde{u}_{,\tilde{y}} + \tilde{v}_{,\tilde{x}}) + \sin(2\phi)(\tilde{v}_{,\tilde{y}} - \tilde{u}_{,\tilde{x}})], \quad (40)$$

and

$$\tilde{\vec{\nabla}} \cdot \underline{\tilde{\sigma}}^V + \tilde{\vec{\nabla}} \cdot \underline{\tilde{\sigma}}^E + \tilde{\vec{\nabla}} \cdot \underline{\tilde{\sigma}}^{\mathrm{ch}} - \tilde{\vec{\nabla}}\tilde{P} = \vec{0}. \quad (41)$$

In these equations, we set $\gamma = \gamma_2/\gamma_1$ and the $\underline{\tilde{\sigma}}$ are the dimensionless stresses. The expressions of the components of $\underline{\tilde{\sigma}}^V$ as a function of ϕ and $\tilde{\vec{v}} = (\tilde{u}, \tilde{v})$ are given in Appendix. In the rest of this section and in the Appendix, and to simplify the notation, we will remove the tilde symbol and assume that we are working with dimensionless variables.

In practice, our numerical code was implemented in C++ using the deal.II finite element library. All the details about it are given in Ref. [43]. We just mention here an important point used to accelerate its convergence. Indeed we noticed that the elastic force could be expressed in the following form:

$$\vec{F}^E = \vec{\nabla} \cdot \underline{\sigma}^E = -\vec{\nabla}\phi\, \Delta\phi - \vec{\nabla} f^i, \quad (42)$$

where

$$f^i = \tfrac{1}{2}(\phi_{,x}^2 + \phi_{,y}^2) \quad (43)$$

is the elastic energy in isotropic elasticity. The elastic force can therefore be rewritten as the sum of the elastic energy gradient and a term proportional to $\Delta\phi$. By grouping the term in energy gradient with the pressure term and by setting $\overline{P} = P + f^i$, and by replacing in the Cauchy equation $\Delta\phi$ by its expression calculated from the torque equation,

$$\Delta\phi(u, v) = \frac{D\phi}{Dt} - 8\pi n + \frac{1}{2}(u_{,y} - v_{,x}) + \frac{\gamma}{2}[\cos(2\phi)(u_{,y} + v_{,x}) + \sin(2\phi)(v_{,y} - u_{,x})], \quad (44)$$

it was possible to greatly improve the code convergence.

To perform the calculations, the values of the nine constants n, X, γ, and the six a_i must be given, knowing that only 6 of them are independent since $a_3 - a_2 = 1$ and $\gamma = a_2 + a_3 = a_6 - a_5$. In practice, we did not know the material constants, in particular, the viscosities which are difficult to measure in smectic-$C^\star$. For this reason, we used a reduced set of viscosities allowing us to qualitatively reproduce our experiments while making the calculations as simple as possible. In the literature two sets of viscosities have been proposed. The first one is due to Pieranski *et al.* [39,57,58] and consists of taking $a_1 = a_5 = a_6 = \gamma = 0$, the "ordinary" viscosity $a_4 > 0$ and $a_2 = -a_3 = -0.5$. With this choice the equations considerably simplify, but they did not allow us to reproduce the experiments, in particular, the complex trajectory of the particle during the transient regime. For this reason, we will not use this model in the following, referring the reader to Ref. [43] for more information about it. The second set of viscosities was proposed by Stannarius *et al.* [59] and consists of taking $a_1 = a_3 = a_6 = 0$, $a_2 = -a_5 = -1$, $a_4 > 0$ and $\gamma = 1$. This choice is more realistic in comparison to the viscosities measured in usual nematics and we will use it because it allowed us to reproduce qualitatively our experiments. In practice, we varied a_4 between 0.5 and 4, X between -5 and $+5$ and n between 0 and 10.

We now describe our results. As before, we start by studying the final state of the system when the phase winding has reached its equilibrium. Figure 24 shows the target patterns and the associated velocity fields calculated for $n = 5$ and $a_4 = 1$ by taking $X = 2.5$ and $X = -2.5$. The first obvious remark is that the number of turns and the shape of the target at equilibrium strongly depends on the sign of X. This is the direct consequence of the flows induced by the Leslie chemohydrodynamical stress in the film. If $X > 0$, then the flows are almost circular and do not deform significantly the target which remains circular in the center. As the flows are counterclockwise, they also favor the phase winding, leading to a number of turns larger than five in the stationary regime. This is obviously not what we have observed as the target remains almost circular in this calculation. The situation is very different when $X < 0$ and much more interesting because the target is this time strongly deformed in its center due to more complex flows with recirculation loops. In that case, the target deforms and becomes oval near the center, in agreement with our observations. This is a clear evidence that the flows induced by the Leslie chemomechanical stress are largely responsible for the central deformation of the target and that X is negative in our system. For completeness, we plotted in Fig. 25 the number of turns in the center of the film divided by n and the magnitude of the maximal velocity in the film in the stationary regime as a function of X for different values of the "ordinary" viscosity a_4. As expected, the larger the viscosity a_4, the less important are the flows and the less the number of turns deviates from n.

In a second step, we studied the role of the flows on the transient regime. Figure 26(a) shows the time evolution of the phase measured in the film center for $X = \pm 2.5$ and $X = 0$ and by neglecting the flows ($\vec{v} = 0$) when $n = 5$. The first remark is that the curve obtained by taking $X = 0$ is not very different from the curve calculated by neglecting the flows ($\vec{v} = 0$). This shows that the backflow effects do not play a considerable role. By contrast, the flows induced by the Leslie chemohydrodynamic stress, in addition to changing the number of turns at equilibrium also changes the shape of the curves, in particular, in the initial regime. Indeed, at $X = 2.5$, the rotation velocity first increases before decreasing when the turns accumulate whereas, at $X = -2.5$, the rotation velocity constantly decreases from the beginning. Figure 26(b) shows the same curves when the phase is scaled with its maximal value reached in the stationary regime. These curves show that the half-winding time is almost the same for $X = 0$ and $X = 2.5$ and is shorter for $X = -2.5$. In all the cases this time is shorter than when the flows are neglected, which shows again that they play an important role in the winding process.

In a third step, we tried to reproduce the complex trajectory of the particle observed during the transient process. Experimentally, we have seen that the particle rotates on

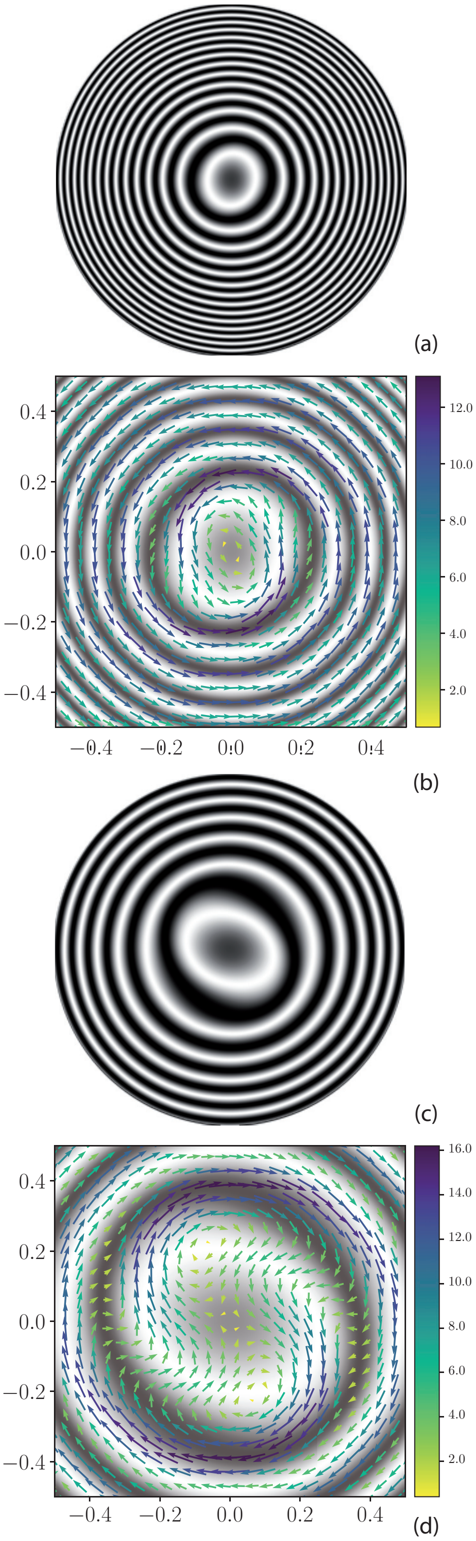

FIG. 24. Target patterns and corresponding velocity fields in the stationary regime when $n = 5$, $a_4 = 1$, $\varepsilon = 0$, and $X = 2.5$ (a, b) and $X = -2.5$ (c, d). Only the central part of the film, where the flows are the most important, is shown in panels (b) and (d), with the texture in background.

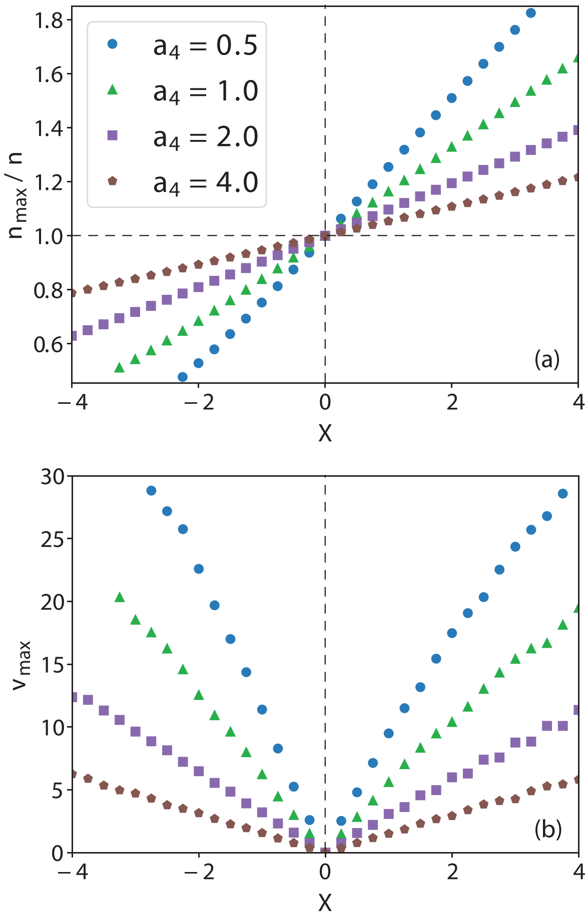

FIG. 25. Number of turns scaled to n in the center of the film (a) and maximal value of the norm of the velocity (b) as a function of X for $n = 5$ and different values of a_4 when the stationary regime is reached. In these simulations, $\varepsilon = 0$.

average clockwise while going back and forth. It is not difficult to convince oneself that this back-and-forth motion is impossible if the flows are everywhere circular as in Fig. 24(b) when X is positive. Conversely, the presence of recirculating vortices in the velocity field of Fig. 24(d) explains this motion when the particle is trapped on one of these vortices. The average rotation of the particle in this case results of a continuous rotation of the velocity field which accompanies the rotation of the director during the transient state.

To reproduce our observation, it would be necessary to calculate the velocity field for a value of n much larger than those we are able to calculate with our computer. It was therefore not directly possible for us to reproduce the experiment. However, we were able to reproduce the observed trajectory in a qualitative way starting from a numerically calculable less wound target. By then rotating this target and the associated velocity field at a constant and well-chosen rate of rotation, it became possible to numerically reconstruct a trajectory that was very similar to the one observed experimentally. The result is shown in Fig. 27 and in Supplemental Movie SM5 [41]. This semiquantitative calculation confirmed that it was well the recirculation vortices coming from the conflict between the backflow effects and the Leslie flows of chemohydrodynamic origin which were responsible for the back-and-forth motion of the particle near the center of the target. This again confirmed that X was negative in our product.

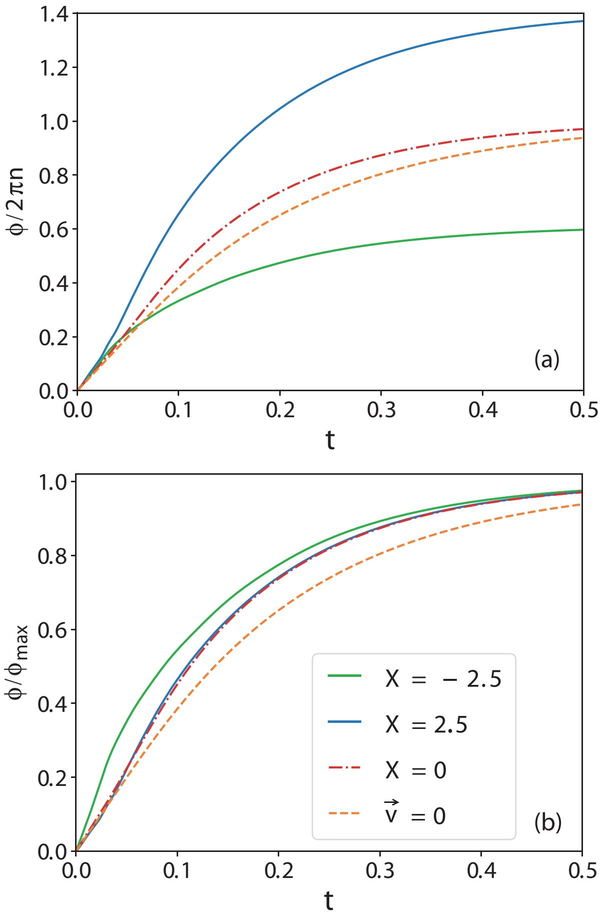

FIG. 26. Number of turns in the center of the film scaled to n (a) or to $n_{\max}$ (b) as a function of the dimensionless time. In these simulations, $n = 5$, $\varepsilon = 0$, and $a_4 = 1$.

C. Phase unwinding

If the flow of alcohol is stopped, then the target unwinds to decrease its elastic energy. The governing equations for the unwinding process are the same as before without the Leslie forcing terms since now $\Delta\mathcal{P} = 0$. As in the previous section, we will proceed by successive approximations to analyze this problem and we will use the dimensionless variables (without the tilde for simplicity).

1. *Analytical solution in isotropic elasticity and in the absence of flow*

In isotropic elasticity and if the backflow is neglected, the torque equation reduces to

$$\frac{\partial\phi}{\partial t} = \Delta\phi = \frac{\partial^2\phi}{\partial^2 r} + \frac{1}{r}\frac{\partial\phi}{\partial r} \qquad (45)$$

in cylindrical coordinates. By taking for initial condition $\phi(0,0) = \phi_{\max}$ and by imposing $\phi(1,t) = 0$ on the edge of the film, the solution is given by

$$\phi(r,t) = \phi_{\max} J_0\left(\frac{r}{\sqrt{\tau}}\right)\exp\left(-\frac{t}{\tau}\right), \qquad (46)$$

where J_0 is the Bessel function of order 0. This equation shows that ϕ decreases exponentially over time with a characteristic time τ given by

$$J_0\left(\frac{1}{\sqrt{\tau}}\right) = 0. \qquad (47)$$

From this equation, the half-unwinding time was deduced: $\tau_{1/2} = \ln(2)\,\tau = 0.12$. In this calculation, the target remains circular over time.

2. *Numerical solution in anisotropic elasticity and in the absence of flow*

Second, we investigated the role of the elastic anisotropy during the unwinding, in the absence of backflow. As the anisotropy makes the problem no longer tractable analytically (angle ϕ now depends on r and the polar angle θ), we solved the torque equation numerically. The resolution was done by using the same method as for the winding. We first calculated the target at equilibrium by taking $n = 5$ and we then calculated its time evolution when the flux of ethanol was stopped. Calculations showed that the target remained almost circular during the relaxation. The curves of the ratio $\phi/\phi_{\max}$ measured in the center of the target as a function of the dimensionless time are shown in Fig. 28 for different values of the anisotropy ε. The corresponding half-unwinding times $\tau_{1/2}$ are reported as a function of ε in Fig. 29. These graphs show that the larger the anisotropy, the slower is the relaxation. This effect is nevertheless not so large since $\tau_{1/2}$ varies from 0.12 to 0.135 when ε varies from 0 ($K_B = K_S$) to 0.8 ($K_B = 9K_S$). Our conclusion is that the anisotropy plays a negligible role during the unwinding, as during the winding. For this reason, we will neglect anisotropy in the following.

3. *Numerical solution in isotropic elasticity and in the presence of flow*

We have seen that flows play an important role during the winding of a target. In this case, however, the flow induced by the chemohydrodynamic force adds to the backflow induced by the rotation of the director. This can lead, when they act in opposite directions, to recirculation vortices responsible for the complex trajectory of the particle observed in Fig. 12. The situation is simpler during the unwinding because only the backflow is present. This case was already analyzed in detail by others, in particular, by Stannarius *et al.* [59] and Pieranski *et al.* [39,57,58]. In practice, we used the same code as before and simulated the unwinding of a target by taking $a_4 = 1$ and starting from a target at equilibrium with $n = 5$. We observed that during the unwinding, the initial oval deformation of the target in the center of the film rapidly disappeared as we can see in the simulation of Fig. 30(b) showing the velocity field and the target in background when it is half unwound. This is well observed experimentally (see the inset in Fig. 17) and due to the fact that the flows induced by the rotation of the director are also circular. Because the fluid and the director rotate in the same sense (here clockwise), the unwinding process is faster when the backflow effects are present. This is clear in Fig. 30(a) where the relaxation curves of the phase in the center of the film are plotted with and without backflow. Note that in this example, $\tau_{1/2}$ passes from 0.15 to 0.12 when the backflow is taken into account.

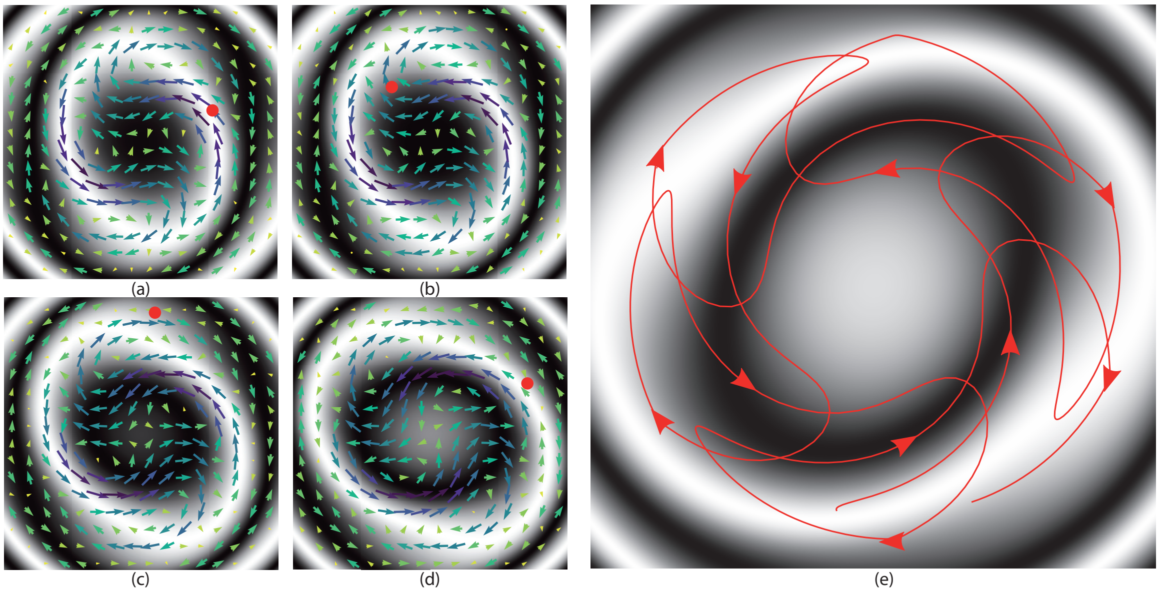

FIG. 27. Simulation of the complex trajectory of the particles. (a)–(d) The red dot shows the position of the particle at different times and the corresponding velocity field. (e) Trajectory of the particle during a full rotation of the director in the center of the film.

Rather than showing more numerical results, we show in the next paragraph that it is possible to make a more complete analytical calculation of this solution without making any assumptions about the viscosities, on the condition of assuming that the target and the streamlines are circular, as suggested by the numerics and the experiments.

4. Approximate analytical solution

In this paragraph, we neglect the elastic anisotropy ($\varepsilon = 0$) but we make no assumptions about the viscosities which we normalize with viscosity γ_1 as before. However, we assume that the phase ϕ and the velocity $\vec{v}$ do not depend on the polar angle θ and are only functions of r and t. Under these conditions the general equations simplify considerably. Again, we use dimensionless variables in this paragraph.

The first equation is the torque equation. In the general case, it is written in the form

$$\frac{D\phi}{Dt} = \Delta\phi + \frac{1}{2}\left(\frac{v_\theta}{r} + \frac{\partial v_\theta}{\partial r}\right) - \frac{\gamma}{2}\cos\left[2(\theta-\phi)\right]\left(\frac{\partial v_\theta}{\partial r} - \frac{v_\theta}{r}\right). \quad (48)$$

If ϕ and $\vec{v}$ are independent of θ, then $\frac{D\phi}{Dt} = \frac{\partial\phi}{\partial t}$ because the fluid particles are advected in a zone where the director keeps the same orientation. In addition, the term in $\cos[2(\theta-\phi)]$ is equal to 0 on average over θ and can be neglected. With these

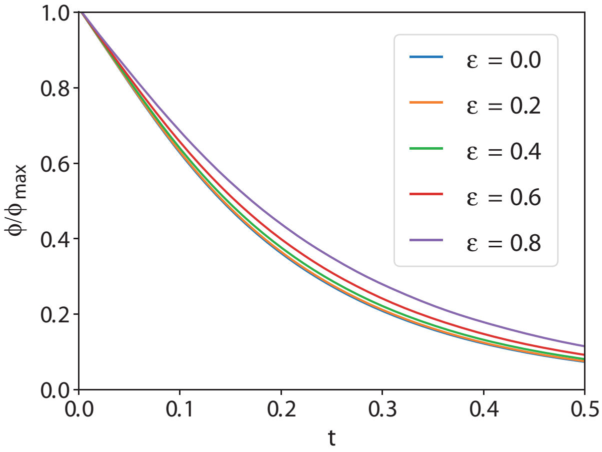

FIG. 28. Angle ϕ in the center of the film scaled by $\phi_{\max}$ as a function of the dimensionless time when the backflow is neglected. Simulations were performed with $n = 5$ for different values of the elastic anisotropy ε. Angle $\phi_{\max} = 2\pi n_{\max}$ corresponds to the initial value of ϕ at the start of the unwinding. $n_{\max}$ is given in Fig. 21.

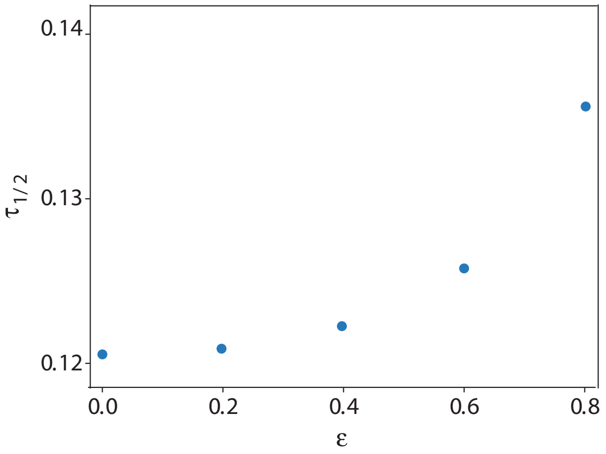

FIG. 29. Half-unwinding time as a function of the elastic anisotropy when the backflow is neglected. These results have been obtained by taking $n = 5$ but it should be emphasized that they depend very little on this value.

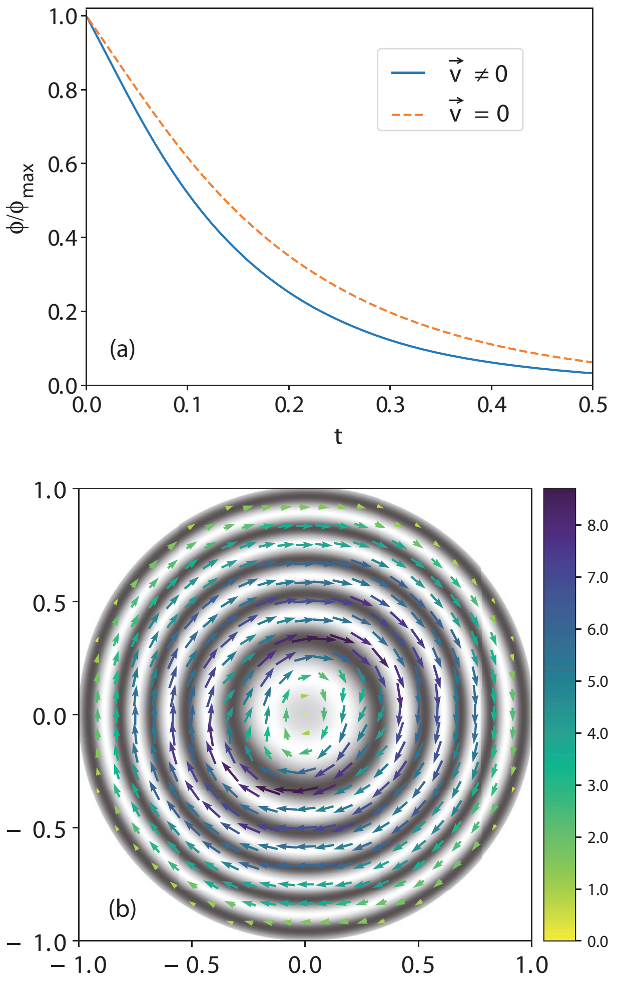

FIG. 30. (a) Normalized phase as a function of the dimensionless time calculated when $\vec{v} = 0$ (dashed line) and $\vec{v} \neq 0$ (solid line) by taking $a_4 = 1$ and $\varepsilon = 0$. At time $t = 0$, $\phi = \phi_{\max} = 10\pi$ (five turns); (b) velocity field when $\phi = \Phi_{\max}/2 = 5\pi$ with the target pattern in background.

simplifications the torque equation becomes

$$\frac{\partial \phi}{\partial t} = \Delta\phi + \frac{1}{2}\left(\frac{v_\theta}{r} + \frac{\partial v_\theta}{\partial r}\right). \tag{49}$$

The second equation is the Cauchy or momentum equation. A simplified integral form of this equation can be found by writing that the momentum of the forces acting on a disk of radius r is equal to zero in the absence of external forces. Note here that we have neglected the inertia of the film, which is justified at low Reynolds number. This equation reads

$$\int_0^{2\pi} r\left(\sigma^V_{\theta r} + \sigma^E_{\theta r}\right) r d\theta + \int_0^{2\pi} \frac{\partial \phi}{\partial r} r d\theta = 0, \tag{50}$$

where the term in the second integral corresponds to the surface elastic torque. From the general expression of the orthoradial component of the viscous and elastic stresses (see Appendix), one obtains after integration over θ the following equation:

$$\overline{\beta}\left(\frac{\partial v_\theta}{\partial r} - \frac{v_\theta}{r}\right) - \frac{1}{2}\frac{\partial \phi}{\partial t} + \frac{1}{4}\left(\frac{v_\theta}{r} + \frac{\partial v_\theta}{\partial r}\right) + \frac{1}{r}\frac{\partial \phi}{\partial r} = 0, \tag{51}$$

where $\overline{\beta}$ is the dimensionless viscosity

$$\overline{\beta} = \frac{a_1}{8} + \frac{a_4}{2} + \frac{a_5}{4} + \frac{a_6}{4}. \tag{52}$$

Note that in the simplified model used before, $\overline{\beta} = a_4/2 + 1/4$. Note also that under this integral form, the pressure term disappears from the momentum equation, while the incompressibility condition becomes

$$\frac{\partial (r v_r)}{\partial r} = 0, \tag{53}$$

which imposes that the radial velocity v_r vanishes.

The solution of Eqs. (49) and (51) can be sought in the form

$$\phi(r, t) = \Phi(r) e^{-t/\tau} \quad \text{and} \quad v_\theta(r, t) = V(r) e^{-t/\tau}. \tag{54}$$

We note now that this form, in particular, the exponential decrease, is compatible with the experimental data when the target is almost circular. With the boundary conditions $\phi(0, 0) = \phi_{\max}$, $\phi(1, t) = 0$, $v_\theta(0, t) = v_\theta(1, t) = 0$ the solution reads

$$\Phi(r) = C J_0\left(\frac{r}{r_0}\right) - \frac{\tau}{T} \tag{55}$$

and

$$V(r) = -\frac{C}{2\overline{\beta} r_0} J_1\left(\frac{r}{r_0}\right) + \frac{r}{T}, \tag{56}$$

where J_0 and J_1 are Bessel functions of zero and first order, respectively, and $r_0 = \sqrt{\tau(1 + \frac{1}{4\overline{\beta}})}$. Note that the condition $V(0) = 0$ is automatically satisfied here and that $V(r) = -4\phi_{\max}(r - r^3)$ when $\overline{\beta} = 0$. The constants τ, T, and C are given by the other boundary conditions which yield

$$\begin{aligned} C - \frac{\tau}{T} &= \phi_{\max}, \\ C J_0\left(\frac{1}{r_0}\right) - \frac{\tau}{T} &= 0, \\ -\frac{C}{2\overline{\beta} r_0} J_1\left(\frac{1}{r_0}\right) + \frac{1}{T} &= 0. \end{aligned} \tag{57}$$

This system can be solved analytically when $\overline{\beta} = 0$. In that case, the solution reads simply

$$\begin{aligned} \phi(r, t) &= \phi_{\max}(1 - r^2) e^{-8t}, \\ v_\theta(r, t) &= -4\phi_{\max}(r - r^3) e^{-8t}. \end{aligned} \tag{58}$$

When $\overline{\beta} \neq 0$, we have found the numerical solution using Mathematica. Note that according to the Ericksen inequalities on viscosities [60], we must always have $\overline{\beta} > -0.25$. In practice, a negative value of $\overline{\beta}$ corresponds to materials with a very low ordinary viscosity, whereas large value of $\overline{\beta}$ corresponds to very viscous materials. Note in passing that making $\overline{\beta}$ infinite in the calculations means neglecting the backflow.

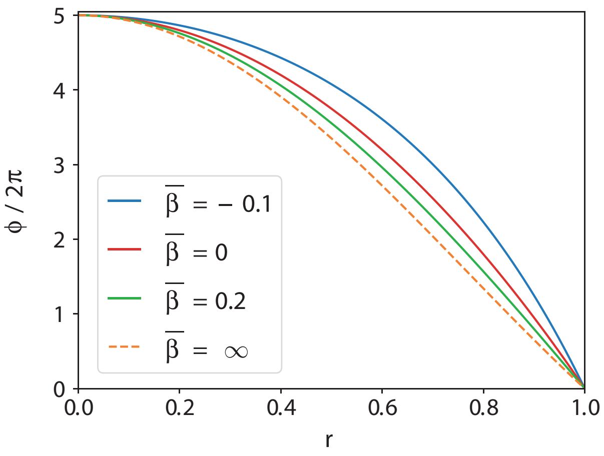

FIG. 31. Phase profiles analytically calculated at $t = 0$ when $\phi = 10\pi$ at the center of the film for different values of $\bar{\beta}$. The elastic anisotropy is neglected ($\varepsilon = 0$). The profiles $\phi(r, t)$ at time t are obtained by multiplying these profiles by $e^{-t/\tau}$.

With these equations, we calculated the phase profile for four values of the viscosity $\overline{\beta}$ when $\phi_{\max} = 10\pi$ in the center of the film (five turns) ($t = 0$ by convention). These profiles are plotted in Fig. 31. Note that the profiles at time t are obtained by multiplying the latter by $\exp(-t/\tau)$ according to Eq. (54). These curves show that the backflow tends to deform the target by widening the homogeneous central zone and by tightening the fringes on the edge of the film. This effect is stronger the smaller $\overline{\beta}$ is and the stronger the backflow is. This is well observed experimentally as can be seen qualitatively in the image of Fig. 17.

We also calculated the velocity profiles for the same values of $\overline{\beta}$. They are plotted in Fig. 32(a). Again the profiles at time t are obtained by multiplying the latter by $\exp(-t/\tau)$. These profiles are all very close to a profile in $r - r^3$ and pass through a maximum (in absolute value) at a distance from the center $r \sim 0.6$. This is compatible with experiment as can be seen in Fig. 18 where the experimental profile was well fitted with a profile in $r - r^3$. Figure 32(b) also shows that $v_{\max}$ strongly increases in absolute value because of the backflow when β decreases and becomes negative.

We also calculated the half-unwinding time $\tau_{1/2} = \ln(2)\,\tau$ as a function of $\overline{\beta}$. The curve is shown in Fig. 33. As expected, we observe that the backflow accelerates the unwinding of the target since $\tau_{1/2}$ decreases when the viscosity $\overline{\beta}$ decreases.

V. COMPARISON BETWEEN THE THEORY AND THE EXPERIMENT

Before concluding, we will estimate the order of magnitude of the material constants in our system. This is complicated because they do not trivially depend on the thickness of the film as we have seen when studying the winding of a target as a function of the thickness. In practice only experiments carried out at the same thickness can be directly compared. This is not the case of all of our experiments. Despite this difficulty we can attempt to give the orders of magnitude of the main constants for 10 layers-thick films for which we have the most data. We will assume that $a_4 = 1$ ($\alpha_4 = \gamma_1$) and $X = -2.5$ since these values explain pretty well the central deformation of the target during the winding.

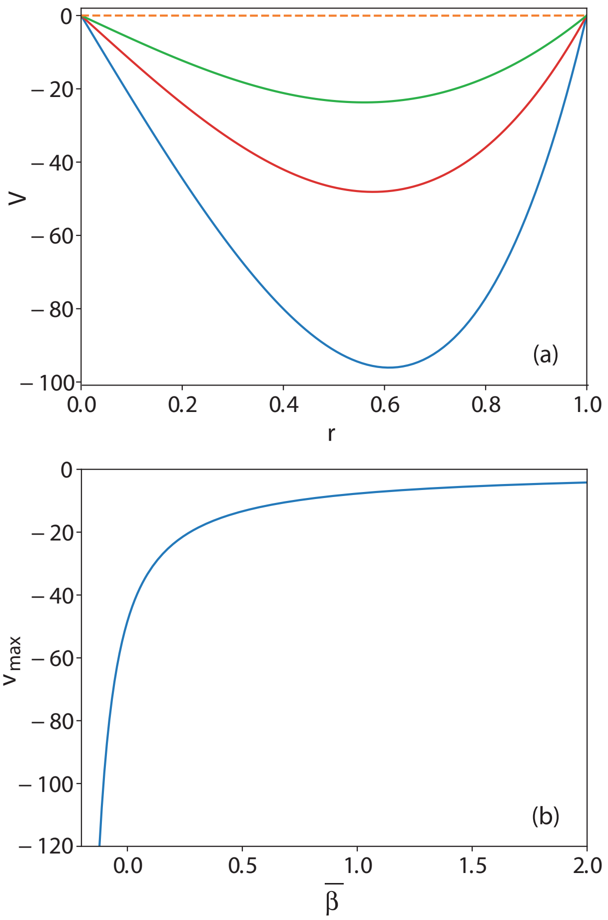

FIG. 32. (a) Velocity profiles analytically calculated at $t = 0$ when $\phi = 10\pi$ at the center of the film for different values of $\bar{\beta}$. The profiles $v_\theta(r, t)$ at time t are obtained by multiplying these profiles by $e^{-t/\tau}$. The elastic anisotropy is neglected ($\varepsilon = 0$). (b) Maximal velocity at time $t = 0$ reached at $r \sim 0.6$ as a function of $\overline{\beta}$.

First, we can give the approximate value of the ratio ν/K. This ratio is given by measuring the slope of the curve in Fig. 15 obtained with a 10 layers-thick film. Correcting for the effect of flows given in Fig. 25(a), we find

$$\frac{\nu}{K} \sim 8.3 \times 10^9\ \mathrm{kPa}^{-1}\mathrm{m}^{-2}.$$

Second, we can give the value of the ratio ν/γ_1. According to Eq. (28), this ratio is given by the slope of the curve in Fig. 11 also obtained with a 10 layers-thick film. Correcting for the effect of flows shown in Fig. 26(b), we find

$$\frac{\nu}{\gamma_1} \sim 2.7 \times 10^9\ \mathrm{kPa}^{-1}\mathrm{s}^{-1}.$$

From these two estimates, we deduce the value of the diffusion coefficient D for a 10 layers-thick film:

$$D \sim 3.2 \times 10^{-4}\ \mathrm{mm}^2\mathrm{s}^{-1}.$$

This value can be compared with the value of D deduced by measuring the half-unwinding time $\tau_{1/2}$ of a target. With the film of Fig. 9 which was also 10-layers thick, we measured

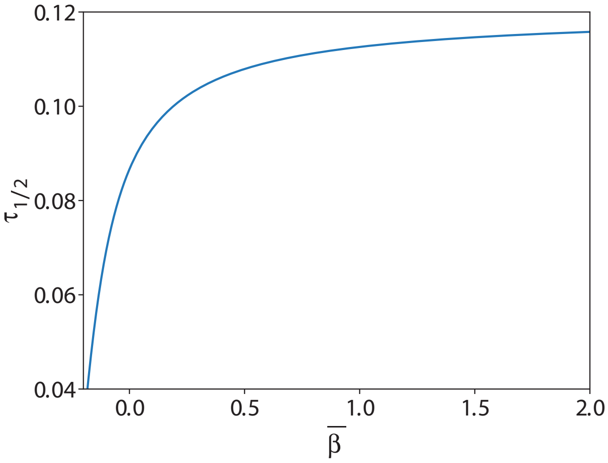

FIG. 33. Half-unwinding time as a function of the dimensionless viscosity $\overline{\beta}$ when $\varepsilon = 0$.

$\tau_{1/2} = 65$ s for $R = 0.56$ mm. By using the value of $\tau_{1/2}$ given in Fig. 33 for $\overline{\beta} = 0.75$ (corresponding to $a_4 = 1$) we found

$$D \sim 1.2\times 10^{-4}\ \mathrm{mm}^2\mathrm{s}^{-1}.$$

This value is smaller than the previous one, but of the same order of magnitude. This difference is not surprising considering the approximations made.

To conclude this paragraph, we can look for the order of magnitude of the velocities during the winding and unwinding of the phase. In our calculations, the velocity is scaled by D/R. By taking for D the average of the values found previously, we find that the reference velocity D/R is about 10^{-3} mm/s for a film of radius 0.25 mm. In the experiment on the trajectory of the particle (Fig. 12), the maximum velocities measured at the center of the target are typically of the order of 0.02 mm/s. In the simulations, the velocities found are of the order of a few tens of D/R (see Fig. 25), i.e., of the order of 0.02–0.03 mm/s, which is well of the right order of magnitude. For the maximum velocity found during the unwinding of a target, we find it to be about 0.03 mm/s from Fig. 18(a) measured with a film of 20 layers when $\phi_{\max} = 10\pi$ (five turns), while the theory predicts a maximum velocity of the order of $7\,D/R$ which gives rather 0.007 mm/s. This value is obviously too small by a factor of 4, even if it is of the good order of magnitude. This last comparison must however be considered with caution because the films used do not have the same thickness and therefore have not necessarily the same diffusivity and more generally the same materials constants.

VI. CONCLUSION

In this article, we have studied the phase winding in a film of smectic-$C^\star$ subjected to a transverse flow of ethanol. We have experimentally shown that when the $+1$ defect imposed by the anchoring conditions at the edge of the film is trapped by the meniscus, a target pattern forms when the film is observed between crossed polarizers. This pattern is due to the winding of the phase ϕ which mainly accumulates in the center of the film, since the director is blocked on the edge of the film due to the anchoring of the molecules on the meniscus. An analogous phenomenon was already observed in Langmuir monolayers when the water evaporates through them. In the two cases, the target formation is mainly due to the existence of a chemomechanical torque predicted by Leslie's theory for chiral materials.

There are, however, important differences between these two systems. In Langmuir monolayers, the targets are circular and flows are strongly damped due to the viscosity of the subphase. In the films, however, the targets are deformed near the center, and flows are present because they are no longer damped by the presence of a subphase.

In practice, these flows could come from a backflow effect. This is indeed what happens during the unwinding of a target, when the flow of ethanol is cut off. In this case, the target is almost circular and the velocity field lines are also circular. As the fluid particles rotate in the same direction as the director, the relaxation is faster, as if the rotational viscosity had decreased. This is a well-known effect in nematics where the backflow makes it possible to reduce the dissipation in the system. By contrast, the situation is very different during the winding process, because we observed more complex flows with recirculation vortices localized near the center of the target. These vortices were revealed by following the trajectory of a particle that accidentally fell onto a target. This experiment showed that the particle rotated on average in the same direction as the director, but also performed a back and forth movement, proving that it was trapped on a recirculation vortex. If the average rotation can be explained in terms of backflow, then it is not the same for this back and forth movement. This experiment therefore revealed the existence of another source of flows, clearly linked to the flow of ethanol since the phenomenon is not observed during the unwinding. In other words, this experiment directly revealed the existence of the Leslie chemohydrodynamical force, also predicted by Leslie's theory for chiral materials. We also observed that the target was strongly deformed in the center during the winding and was almost circular during the unwinding. This observation suggested that the deformation of the target was not due to elastic anisotropy, but rather to the existence of these recirculation vortices.

To explain these observations, we wrote the equations that govern the dynamics of the films, taking into account the chemomechanical and chemohydrodynamical coupling terms of Leslie. We then solved these equations, analytically in simple cases when the elastic anisotropy and the flows are neglected, and numerically, when one of these two effects is taken into account. We showed that the elastic anisotropy alone could not explain the deformation of the targets during the winding, according to our observations. For this reason and to simplify the calculations, we neglected the anisotropy when we studied the flows. We also used an approximate model for the viscosities due to Stannarius *et al.*, as they are all unknown in our system. With this model, we were able to show that recirculation vortices develop in the center of the film only when the two coefficients ν and μ describing the chemical Leslie effects are of opposite signs ($X < 0$). More precisely, the observation of the direction of rotation of the director in our experiments showed us that, with our definitions, the thermomechanical coefficient ν is positive while the thermohydrodynamical coefficient μ is negative.

If the agreement between experiment and theory is qualitatively good, there are still problems to explain quantitatively all of our observations.

The first difficulty was the near impossibility to do all measurements with films of the same thickness. From this point of view, it would be very interesting to develop a method to thin the films in a controlled way like the one used in Ref. [61] by locally heating the film with a heating wire. This method is, however, difficult to implement here because the FELIX mixture melts at high temperature and, also, for technical reasons related to the difficulty of introducing the heating wire under the film in the experimental device used to control the flow of ethanol.

The second difficulty came from the complexity of the model itself and from the large number of material constants. In particular, the approximations made on the viscosity tensor are certainly too simplistic. This problem is unfortunately difficult to improve without any additional information on the different viscosities. Solving the equations taking into account both the elastic anisotropy and the flows could also improve things, but this problem is complicated numerically because the weak formulation of the anisotropic elastic terms is particularly difficult. It would also be important to change the boundary conditions in our numerics by introducing a defect near the edge of the film. This could certainly explain why it was impossible to wind a target at very low ethanol flow.

Nevertheless, there is no doubt that in our system μ and ν are of opposite signs and of the same order of magnitude, to within a factor of 2 or 3. This result is important and confirms our intuition that the differences of several orders of magnitude reported in the literature between the thermomechanical and thermohydrodynamical coefficients of Akopyan and Zel'dovich in nematics are likely due to artifacts (for an in-depth discussion of this issue, see Ref. [19]).

ACKNOWLEDGMENTS

The authors warmly thank G. Poy for his help in the exact calculation of the Leslie chemical terms in films and A. Dequidt and J. Ignés-Mullol for a critical reading of the manuscript and useful comments.

APPENDIX: COMPONENTS OF THE STRESS TENSOR IN CARTESIAN AND CYLINDRICAL COORDINATES

We first give the components of the viscous stress tensor in cartesian coordinates:

$$\begin{aligned}\sigma^V_{xx} &= [a_4 + (a_5 + a_6 + a_1\cos^2\phi)\cos^2\phi]u_{,x} + \frac{a_1}{4}\sin^2(2\phi)v_{,y} + \left(\frac{a_1}{2}\cos^2\phi + \frac{a_5+a_6}{4}\right)\sin(2\phi)(v_{,x}+u_{,y})\\ &\quad + \frac{a_2+a_3}{2}\sin(2\phi)\left[-\frac{D\phi}{Dt} + \frac{1}{2}(v_{,x}-u_{,y})\right],\end{aligned} \tag{A1}$$

$$\begin{aligned}\sigma^V_{yy} &= [a_4 + (a_5 + a_6 + a_1\sin^2\phi)\sin^2\phi]v_{,y} + \frac{a_1}{4}\sin^2(2\phi)u_{,x} + \left(\frac{a_1}{2}\sin^2\phi + \frac{a_5+a_6}{4}\right)\sin(2\phi)(v_{,x}+u_{,y})\\ &\quad + \frac{a_2+a_3}{2}\sin(2\phi)\left[\frac{D\phi}{Dt} - \frac{1}{2}(v_{,x}-u_{,y})\right],\end{aligned} \tag{A2}$$

$$\begin{aligned}\sigma^V_{xy} &= \left[\frac{a_4}{2} + \frac{a_5}{2}\sin^2\phi + \frac{a_6}{2}\cos^2\phi + \frac{a_1}{4}\sin^2(2\phi)\right](v_{,x}+u_{,y}) + \left[\frac{a_5}{2}\sin(2\phi) + \frac{a_1}{2}\sin(2\phi)\cos^2\phi\right]u_{,x}\\ &\quad + \left(\frac{a_6}{2}\sin(2\phi) + \frac{a_1}{2}\sin(2\phi)\sin^2\phi\right)v_{,y} + (a_3\cos^2\phi - a_2\sin^2\phi)\left[\frac{D\phi}{Dt} - \frac{1}{2}(v_{,x}-u_{,y})\right],\end{aligned} \tag{A3}$$

$$\begin{aligned}\sigma^V_{yx} &= \left[\frac{a_4}{2} + \frac{a_5}{2}\cos^2\phi + \frac{a_6}{2}\sin^2\phi + \frac{a_1}{4}\sin^2(2\phi)\right](v_{,x}+u_{,y}) + \left[\frac{a_5}{2}\sin(2\phi) + \frac{a_1}{2}\sin(2\phi)\sin^2\phi\right]v_{,y}\\ &\quad + \left[\frac{a_6}{2}\sin(2\phi) + \frac{a_1}{2}\sin(2\phi)\cos^2\phi\right]u_{,x} + (a_2\cos^2\phi - a_3\sin^2\phi)\left[\frac{D\phi}{Dt} - \frac{1}{2}(v_{,x}-u_{,y})\right].\end{aligned} \tag{A4}$$

In cylindrical coordinates, we only need the expressions of $\sigma^E_{\theta r}$ and $\sigma^V_{\theta r}$ to derive Eq. (51). They read as follows in isotropic elasticity and by assuming that the velocity is independent of θ:

$$\sigma^E_{\theta r} = -\frac{K}{r}\frac{\partial\phi}{\partial r}\frac{\partial\phi}{\partial\theta} \tag{A5}$$

and

$$\begin{aligned}\sigma^V_{\theta r} &= \left\{\frac{\alpha_4}{2} + \frac{\alpha_5}{2}\cos^2(\theta-\phi) + \frac{\alpha_6}{2}\sin^2(\theta-\phi) + \frac{\alpha_1}{4}\sin^2[2(\theta-\phi)]\right\}\left(\frac{\partial v_\theta}{\partial r} - \frac{v_\theta}{r}\right)\\ &\quad + [\alpha_2\cos^2(\theta-\phi) - \alpha_3\sin^2(\theta-\phi)]\left[\frac{D\phi}{Dt} - \frac{1}{2}\left(\frac{v_\theta}{r} + \frac{\partial v_\theta}{\partial r}\right)\right].\end{aligned} \tag{A6}$$

For completeness, we also give the component $\sigma^L_{\theta r}$ of the chemohydrodynamical stress:

$$\sigma^L_{\theta r} = -\frac{\mu \Delta \mathcal{P}}{2} \cos[2(\theta - \phi)]. \tag{A7}$$

[1] O. Lehmann, Structur, System und magnetisches Verhalten flüssiger Krystalle und deren Mischbarkeit mit festen, Ann. Phys. **307**, 649 (1900).

[2] O. Lehmann, *Flüssige Krystalle und ihr scheinbares Leben* (Verlag von Leopod Voss, Hamburg, 1921)

[3] F. M. Leslie, Some thermal effects in cholesteric liquid crystals, Proc. R. Soc. London A **307**, 359 (1968).

[4] P. Oswald and A. Dequidt, Direct measurement of the thermomechanical Lehmann coefficient in a compensated cholesteric liquid crystal, Europhys. Lett. **83**, 16005 (2008).

[5] P. Oswald, Lehmann rotation of cholesteric droplets subjected to a temperature gradient: Role of the concentration of chiral molecules, Eur. Phys. J. E **28**, 377 (2009).

[6] J. Yoshioka, F. Ito, Y. Suzuki, H. Takahashi, H. Takizawa, and Y. Tabe, Director/barycentric rotation in cholesteric droplets under temperature gradient, Soft Matter **10**, 5869 (2014).

[7] T. Yamamoto, M. Kuroda, and M. Sano, Three-dimensional analysis of thermomechanically rotating cholesteric liquid crystal droplets under a temperature gradient, Europhys. Lett. **109**, 46001 (2015).

[8] P Oswald, About the Leslie explanation of the Lehmann effect in cholesteric liquid crystals, Europhys. Lett. **97**, 36006 (2012).

[9] P Oswald, Microscopic vs. macroscopic origin of the Lehmann effect in cholesteric liquid crystals, Eur. Phys. J. E **35**, 10 (2012).

[10] P. Oswald, Leslie thermomechanical power in diluted cholesteric liquid crystals, Europhys. Lett. **108**, 36001 (2014).

[11] J. Ignés-Mullol, G. Poy, and P. Oswald, Continuous Rotation of Achiral Nematic Liquid Crystal Droplets Driven by Heat Flux, Phys. Rev. Lett. **117**, 057801 (2016).

[12] K. S. Krishnamurthy, D. S. Shankar Rao, S. Sharma, and C. V. Yelamaggad, Structure, stability, and electro-optic features of nematic drops in 1″, 7″-bis (4-cyanobiphenyl-4′-yl) heptane–surfactant binary systems, Phys. Rev. E **105**, 024709 (2022).

[13] P. Oswald, G. Poy, and K. S. Krishnamurthy, Structure and Lehmann rotation of drops in a surfactant-doped bent-core liquid crystal, Phys. Rev. E **106**, 024705 (2022).

[14] N. Éber and I. Jánossy, An experiment on the thermomechanical coupling in cholesterics, Mol. Cryst. Liq. Cryst. **72**, 233 (1982).

[15] N. Éber and I. Jánossy, Thermomechanical coupling in compensated cholesterics, Mol. Cryst. Liq. Cryst. **102**, 311 (1984).

[16] N. Éber and I. Jánossy, Note on "macroscopic description of compensated cholesteric and chiral smectic liquid crystals", Mol. Cryst. Liq. Cryst., Lett. **5**, 81 (1988).

[17] A. Dequidt and P. Oswald, Lehmann effect in compensated cholesteric liquid crystals, Europhys. Lett. **80**, 26001 (2007).

[18] A. Dequidt, A. Żywociński, and P. Oswald, Lehmann effect in a compensated cholesteric liquid crystal: Experimental evidence with fixed and gliding boundary conditions, Eur. Phys. J. E **25**, 277 (2008).

[19] P. Oswald, A. Dequidt, and G. Poy, Thermomechanical effects in liquid crystals, in *Liquid Crystals: New Perspectives*, edited by P. Pieranski and M. H. Godinho (Wiley, Hoboken, NJ, 2021), p. 117.

[20] P. G. de Gennes and J. Prost, *The Physics of Liquid Crystals*, International Series of Monographs on Physics (Clarendon Press, Oxford, UK, 1995).

[21] H. P. Padmini and N. V. Madhusudana, Electromechanical effect in cholesteric mixtures with a compensation temperature, Liq. Cryst. **14**, 497 (1993).

[22] A. Dequidt and P. Oswald, Does the electric Lehmann effect exist in cholesteric liquid crystals? Eur. Phys. J. E **24**, 157 (2007).

[23] Y. Tabe and H. Yokoyama, Coherent collective precession of molecular rotors with chiral propellers, Nat. Mater. **2**, 806 (2003).

[24] J. Adams, W. Rettig, R. S. Duran, J. Naciri, and R. Shashidhar, Langmuir films of liquid crystalline materials: the influence of molecular architecture on morphology and properties, J. Phys. Chem. **97**, 2021 (1993).

[25] G. Watanabe, S. Ishizaki, and Y. Tabe, Collective precession of chiral liquid crystals under transmembrane mass flow, in *Physics of Self-Organization Systems* (World Scientific, Singapore, 2008), p. 138.

[26] M. Yoneya, Y. Tabe, and H. Yokoyama, Molecular dynamics simulation of condensed-phase chiral molecular propellers, J. Phys. Chem. B **114**, 8320 (2010).

[27] Y. Tsori and P.-G. de Gennes, Frustrated rotations in nematic monolayers, Eur. Phys. J. E **14**, 91 (2004).

[28] D. Svenšek, H. Pleiner, and H. R. Brand, Phase Winding in Chiral Liquid Crystalline Monolayers due to Lehmann Effects, Phys. Rev. Lett. **96**, 140601 (2006).

[29] R. K. Gupta, K. A. Suresh, S. Kumar, L. M. Lopatina, R. L. B. Selinger, and J. V. Selinger, Spatiotemporal patterns in a Langmuir monolayer due to driven molecular precession, Phys. Rev. E **78**, 041703 (2008).

[30] P. Milczarczyk-Piwowarczyk, A. Żywociński, K. Noworyta, and R. Hołyst, Collective rotations of ferroelectric liquid crystals at the air/water interface, Langmuir **24**, 12354 (2008).

[31] P. Nitoń, A. Żywociński, M. Fiałkowski, and R. Hołyst, A "nano-windmill" driven by a flux of water vapour: a comparison to the rotating ATPase, Nanoscale **5**, 9732 (2013).

[32] F. Bunel, J. Ignés-Mullol, F. Sagués, and P. Oswald, Chemical Leslie effect in Langmuir monolayers: A complete experimental characterization, Soft Matter **14**, 4835 (2018).

[33] S. Kazuyoshi, U. Ken, U. Kazuhisa, T. Kazumasa, and Y. Tabe, Lehmann force acting on a microparticle in smectic-C* free-standing films subjected to methanol vapor transport, Jpn. J. Appl. Phys. **50**, 125804 (2011).

[34] K. Seki, K. Ueda, Y. Okumura, and Y. Tabe, Nonequilibrium dynamics of 2D liquid crystals driven by transmembrane gas flow, J. Phys.: Condens. Matter **23**, 284114 (2011).

[35] F. Bunel and P. Oswald, Chemical Leslie effect in a chiral smectic-C* film: Singular target patterns, Phys. Rev. E **107**, 024704 (2023).

[36] P. E. Cladis, Y. Couder, and H. R. Brand, Phase Winding and Flow Alignment in Freely Suspended Films of Smectic-*C* Liquid Crystals, Phys. Rev. Lett. **55**, 2945 (1985).

[37] I. Jánossy, Diffusomechanical coupling in cholesteric liquid crystals, J. Phys. Lett. Paris **42**, 41 (1981).

[38] S. Kundu, P. Nayek, T. Ray, T. P. Majumder, S. K. Roy, and S. Kobayashi, Influence of network stabilization on the dielectric and electrooptical properties of ferroelectric liquid crystal FELIX-M4851/100, Jpn. J. Appl. Phys. **48**, 061501 (2009).

[39] P. Oswald and P. Pieranski, *Smectic and Columnar Liquid Crystals: Concepts and Physical Properties Illustrated by Experiments*, Liquid Crystals Book Series (CRC Press, Taylor & Francis, Boca Raton, FL, 2005).

[40] S. T. Lagerwall, *Ferroelectric and Antiferroelectric Liquid Crystals* (Wiley, Hoboken, NJ, 1999).

[41] See Supplemental Material at http://link.aps.org/supplemental/10.1103/PhysRevE.107.024703 for all movies related to instances in the article.

[42] See Refs. [35,43] for the description of a new method allowing to locally measure the flow velocity in the film without introducing particles into the film.

[43] F. Bunel, Effet Leslie chimique dans les monocouches de Langmuir et les films libres de smectique C chiraux, Ph.D. thesis, Ecole Normale Supérieure de Lyon, Lyon (2021).

[44] K. Okano, Electrostatic contribution to the distortion free energy density of ferroelectric liquid crystals, Jpn. J. Appl. Phys. **25**, L846 (1986).

[45] J.-B. Lee, R. A. Pelcovits, and R. B. Meyer, Role of electrostatics in the texture of islands in freestanding ferroelectric liquid crystal films, Phys. Rev. E **75**, 051701 (2007).

[46] P. V. Dolganov, V. K. Dolganov, and P. Cluzeau, The effect of spontaneous polarization on two-dimensional elasticity of smectic liquid crystals, J. Exp. Theor. Phys. **116**, 1043 (2013).

[47] Werner Martienssen and Hans Warlimont, *Springer Handbook of Condensed Matter and Materials Data* (Springer Science & Business Media, Cham, 2006).

[48] I. W. Stewart, *The Static and Dynamic Continuum Theory of Liquid Crystals: A Mathematical Introduction*, Liquid Crystals Book Series (CRC Press, Boca Raton, FL, 2004).

[49] O. Parodi, Stress tensor for a nematic liquid crystal, J. Phys. Paris **31**, 581 (1970).

[50] R. S. Akopyan and B. Ya. Zel'dovich, Thermomechanical effects in deformed nematics, JETP **60**, 953 (1984).

[51] G. Poy and P. Oswald, On the existence of the thermomechanical terms of Akopyan and Zel'dovich in cholesteric liquid crystals, Liq. Cryst. **45**, 1428 (2018).

[52] G. Poy, F. Bunel, and P. Oswald, Theory of the Leslie and Akopyan and Zel'dovich chemomechanical and chemohydrodynamical effects in freestanding and supported films of SmC and SmC* phases (to be published).

[53] This boundary condition will be used throughout this paper to simplify the calculations, although it is not realistic since a planar anchoring of the director is observed at the edge of the film, producing a +1 defect. Our calculations and our simulations will therefore be strictly valid only in the limit of "large" numbers of turns, when the dislocation which forms in the fringe network at the location of the +1 defect is strongly localized at the edge of the film, as can be seen in Figs. 13 and 17.

[54] D. Arndt, W. Bangerth, B. Blais, T. C. Clevenger, M. Fehling, A. V. Grayver, T. Heister, L. Heltai, M. Kronbichler, M. Maier, P. Munch, J.-P. Pelteret, R. Rastak, I. Thomas, B. Turcksin, Z. Wang, and D. Wells, The `deal.II` library, version 9.2, J. Num. Math. **28**, 131 (2020).

[55] G. Poy, F. Bunel, and P. Oswald, Role of anchoring energy on the texture of cholesteric droplets: Finite-element simulations and experiments, Phys. Rev. E **96**, 012705 (2017).

[56] M. Kronbichler, T. Heister, and W. Bangerth, High accuracy mantle convection simulation through modern numerical methods, Geophys. J. Int. **191**, 12 (2012).

[57] C. Chevallard, J.-M. Gilli, T. Frisch, I. V. Chikina, and P. Pieranski, Magic spiral submitted to a torque: Topological flows driven by Ericksen stresses in Sm-C films, Mol. Cryst. Liq. Cryst. Sci. Technol. Sect. A **328**, 595 (1999).

[58] C. Chevallard, J.-M. Gilli, T. Frisch, I. V. Chikina, and P. Pieranski, Cladis' orbiting disclinations in smectic films submitted to a torque, Mol. Cryst. Liq. Cryst. Sci. Technol. Sect. A **328**, 589 (1999).

[59] K. Harth, A. Eremin, and R. Stannarius, Vortex flow in freestanding smectic-*C* films driven by elastic distortions, Soft Matter **7**, 2858 (2011).

[60] T. Carlsson, F. M. Leslie, and N. A. Clark, Macroscopic theory for the flow behavior of smectic-*C* and smectic-*C** liquid crystals, Phys. Rev. E **51**, 4509 (1995).

[61] J.-C. Géminard, R. Hołyst, and P. Oswald, Meniscus and Dislocations in Freestanding Films of Smectic-*A* Liquid Crystals, Phys. Rev. Lett. **78**, 1924 (1997).